

מכון ויצמן למדע

WEIZMANN INSTITUTE OF SCIENCE



Tumor-reactive antibodies evolve from non-binding and autoreactive precursors

Document Version:

Accepted author manuscript (peer-reviewed)

Citation for published version:

Mazor, RD, Nathan, N, Gilboa, A, Stoler-Barak, L, Moss, L, Solomonov, I, Hanuna, A, Divinsky, Y, Shmueli, MD, Hezroni, H, Zaretsky, I, Mor, M, Golani, O, Sabah, G, Jakobson-Setton, A, Yanichkin, N, Feinmesser, M, Tsoref, D, Salman, L, Yeoshoua, E, Peretz, E, Erlich, I, Mendelson Cohen, N, Gershoni, JM, Freund, N, Merbl, Y, Yaari, G, Eitan, R, Sagi, I & Shulman, Z 2022, 'Tumor-reactive antibodies evolve from non-binding and autoreactive precursors', *Cell*, vol. 185, no. 7, pp. 1208-1222. <https://doi.org/10.1016/j.cell.2022.02.012>

Total number of authors:

30

Digital Object Identifier (DOI):

[10.1016/j.cell.2022.02.012](https://doi.org/10.1016/j.cell.2022.02.012)

Published In:

Cell

License:

Other

General rights

@ 2020 This manuscript version is made available under the above license via The Weizmann Institute of Science Open Access Collection is retained by the author(s) and / or other copyright owners and it is a condition of accessing these publications that users recognize and abide by the legal requirements associated with these rights.

How does open access to this work benefit you?

Let us know @ library@weizmann.ac.il

Take down policy

The Weizmann Institute of Science has made every reasonable effort to ensure that Weizmann Institute of Science content complies with copyright restrictions. If you believe that the public display of this file breaches copyright please contact library@weizmann.ac.il providing details, and we will remove access to the work immediately and investigate your claim.

Tumor-reactive antibodies evolve from non-binding and autoreactive precursors

Roei D. Mazor^{1,2}, Nachum Nathan¹, Amit Gilboa³, Liat Stoler-Barak¹, Lihee Moss¹, Inna Solomonov², Assaf Hanuna², Yalin Divinsky¹, Merav D. Shmueli¹, Hadas Hezroni¹, Irina Zaretzky^{1,4}, Michael Mor⁵, Ofra Golani⁴, Gad Sabah^{6,9}, Ariella Jakobson-Setton^{6,9}, Natalia Yanichkin^{7,9}, Meora Feinmesser^{7,9}, Daliah Tsoref^{8,9}, Lina Salman^{6,9}, Effi Yeoshoua^{6,9}, Eyal Peretz⁶, Inna Erlich⁶, Netta Mendelson Cohen¹⁰, Jonathan M. Gershoni¹¹, Natalia Freund⁵, Yifat Merbl¹, Gur Yaari³, Eitan Ram^{5,6}, Irit Sagi^{2*} and Ziv Shulman^{1,12*}

¹Department of Immunology, Weizmann Institute of Science, Rehovot 7610001, Israel

²Department of Biological Regulation, Weizmann Institute of Science, Rehovot 7610001, Israel

³Faculty of Engineering, Bar Ilan University, Ramat Gan 52900, Israel.

⁴Department of Life Sciences and Core Facilities, Weizmann Institute of Science, Rehovot 7610001, Israel.

⁵Department of Clinical Microbiology and Immunology, Sackler Faculty of Medicine, Tel Aviv University, Tel Aviv-Yafo, Israel

⁶Gynecologic Oncology Division, Helen Schneider Hospital for Women, Rabin Medical Center, Petah-Tikva, Israel.

⁷Department of Pathology, Rabin Medical Center, Petah Tikva, Israel.

⁸Davidoff Cancer Center, Rabin Medical Center, Petah Tikva, Israel.

⁹The Sackler School of Medicine, Tel Aviv University, Tel Aviv, Israel.

¹⁰Department of Mathematics and Computer Science, Weizmann Institute of Science, Rehovot 7610001, Israel

¹¹Department of Cell Research and Immunology, George S. Wise Faculty of Life Sciences, Tel Aviv University, Tel Aviv, Israel

¹²Lead contact

*Corresponding authors and lead contacts: ziv.shulman@weizmann.ac.il, irit.sagi@weizmann.ac.il

Summary

The tumor microenvironment hosts antibody-secreting cells (ASCs) associated with a favorable prognosis in several types of cancer. Patient-derived antibodies have diagnostic and therapeutic potential; yet, it remains unclear how antibodies gain autoreactivity and target tumors. Here, we found that somatic hypermutations (SHMs) promote antibody anti-tumor reactivity against surface autoantigens in high grade serous ovarian carcinoma (HGSOC). Patient-derived tumor cells were frequently coated with IgGs. Intratumoral ASCs in HGSOC were both mutated and clonally expanded, and produced tumor-reactive antibodies that targeted MMP14, which is abundantly expressed on the tumor cell surface. Reversion of monoclonal-antibodies to their germline configuration revealed two types of classes: one dependent on SHMs for tumor binding, and a second with germline-encoded autoreactivity. Thus, tumor-reactive autoantibodies are either naturally occurring or evolve through an antigen-driven selection process. These findings highlight the origin and potential applicability of autoantibodies directed at surface antigens for tumor targeting in cancer patients.

Introduction

Antigen driven selection of B cells bearing high-affinity antibodies for clonal expansion and differentiation in germinal centers (GCs) in response to infection or vaccination has been extensively studied (Victora and Nussenzweig 2012). In cancer patients, autoreactive antibodies are frequently present, suggesting that a breach of self tolerance takes place, as observed in autoimmune diseases (Zaenker, Gray, and Ziman 2016). Yet, our knowledge regarding the cellular mechanisms underlying the production of tumor-reactive autoantibodies and their cell surface antigens remains elusive. Intratumoral antibody secreting cells (ASCs) and their B cell precursors were described in many types of solid tumors, and the presence of B cell-rich tertiary lymphoid structures (TLS) was robustly associated with a superior prognosis, and was shown to predict a beneficial response to immunotherapy treatments (Petitprez et al. 2020; Helmink et al. 2020; Cabrita et al. 2020; Nelson 2010; Kroeger, Milne, and Nelson 2016; Pitzalis et al. 2014). Intratumoral B cells can support an anti-tumor immune response through several mechanisms, including antigen presentation to T cells (Cui et al., n.d.) and differentiation to ASCs that secrete self-reactive and tumor-specific antibodies (Sharonov et al. 2020; Wieland et al. 2020). While many studies characterized the B cell subtypes and ASCs that reside in various tumors (Maletzki et al. 2012; Kroeger, Milne, and Nelson 2016; Bolotin et al. 2017; Saul et al. 2016; Nzula, Going, and Stott 2003; Mose et al. 2016; Montfort et al. 2017), generation of monoclonal antibodies and comprehensive analysis of their origin, specificity and function remains a challenge in cancers that lack defined surface immunogens (Wieland et al. 2020).

Intratumoral B cells and ASCs are frequently observed in ovarian tumors (Nelson 2010; Montfort et al. 2017). In this desmoplastic cancer, the tumor mass, its highly fibrotic microenvironment, and metastatic cells are constantly in contact with ascites fluids that accumulate antibodies which are produced by ASCs in the tumor microenvironment (Rao, Subba Rao, and Hanjani 1988; Silburn

et al. 1984). Since these tumor-associated fluids are very accessible, this type of cancer is ideal for analysis of the anti-tumor humoral immune response (Rao, Subba Rao, and Hanjani 1988; Silburn et al. 1984). High-grade serous ovarian carcinoma (HGSOC) is the most prevalent subtype of ovarian cancer (Bowtell 2010; Ramalingam 2016; Jayson et al. 2014) and treatment generally includes a combination of chemotherapy and surgery, whereas biological treatment alternatives are scarce and include primarily anti-VEGF therapy and poly ADP-ribose polymerase (PARP) inhibitors (Mahmood et al. 2020). Specifically, manipulation of the immune response through administration of checkpoint inhibitors has not shown strong beneficial effects to date (Doo, Norian, and Arend 2019; Boland et al. 2019), emphasizing the need for a deeper understanding of the immune response against this specific tumor.

In HGSOC patients, the tumor's extracellular matrix (ECM) plays a pivotal role in promoting malignancy, as it supports cell growth and invasiveness (Cho, Howell, and Colvin 2015). The malignant ECM is often highly fibrotic and constantly modulated by ECM-remodeling enzymes such as matrix metalloproteinases (MMPs), including MMP14 (MT1-MMP), which is highly expressed on HGSOC cell surface (Kamel et al. 2010; Cathcart et al. 2016; Maria Caroline Vos et al. 2016; Sakata et al. 2000; M. Caroline Vos et al. 2021). Overexpression of tumor self-proteins was suggested to drive autoantibody generation (Zaenker, Gray, and Ziman 2016; Milne et al. 2008; Ma et al. 2020) and it was shown that antibodies directed against MMPs emerge under different pathological conditions, suggesting that this enzyme family may trigger an immune response in cancer (Crowley et al. 2016; Sato et al. 2003; Nishijima et al. 2004; Wang et al. 2020; Gnjjatic et al. 2010).

Here, using large-scale tumor-section imaging, patient derived monoclonal antibodies and tumor target identification, we demonstrate that somatic hypermutations (SHM) promote antibody

reactivity to surface antigens in HGSOC patients in parallel to germline-encoded tumor-binding immunoglobulins.

Results

The tumor cell surface is targeted by endogenous antibodies in cancer patients

IgG autoantibodies that primarily bind intracellular targets were described in HGSOC and other types of cancer (Hu et al. 2019; Sharonov et al. 2020; Ran, Klein, and Witz 1976; Witz 1977), but whether endogenous antibodies can directly bind tumor surfaces *in situ* was never systematically examined in a large patient cohort. To this end, we examined 34 tumor samples collected from HGSOC patients who had not yet received neoadjuvant chemotherapy, and 17 healthy ovary and fallopian tube tissue samples. Formalin-fixed paraffin-embedded (FFPE) specimens were stained with H&E and reviewed in a blinded manner by a certified pathologist specializing in gynecologic pathology, to assure adequate sample quantity and quality (**Figure 1A and Supplementary Table S1**). Healthy samples from the female reproductive tract were histologically validated after being obtained from non-diseased contralateral adnexa of patients undergoing surgery, as well as from 9 patients in the cohort whose final pathological diagnosis ruled out HGSOC. In order to visualize the maximal area in tumor sections and avoid topological biases, we systematically imaged large sections of tumors (1.1-5.12 cm²) that were stained with anti-IgG fluorescent antibodies, using a slide scanner (**Supplementary Figure S1A**). In the majority of the patient samples, IgG positive tumor cells were primarily located in proximity to the vascular stroma as well as the papillary areas of the tumor (**Figure 1A**). To precisely quantify the frequency of IgG-bound epithelial cells, we used a machine learning approach, QuPath (Bankhead et al. 2017), to differentiate between stromal, epithelial, and immune cells based on multiple histological features including nuclear shape, size and chromatin density. This technique allowed us to quantify the number of IgG coated cells per slide, and determine their frequency in the sample. The malignant epithelial cells are

thought to arise from either the fallopian tube epithelium (Bowtell 2010; Labidi-Galy et al. 2017; DeWeerd 2021) or from the ovarian surface epithelium (Auersperg 2013). Therefore, we used both fallopian tube and ovarian surface epithelial cells as healthy control tissues. **(Figure 1A and Supplementary Figure S1A)**. The percentages of IgG coated cells out of the total epithelial cells in the sample for each patient or healthy control are shown in Figure 1B. The majority (61%) of the analyzed HGSOC primary tumor specimens showed epithelial cell antibody coating above background levels observed in healthy fallopian tube and ovarian surface epithelium **(Figure 1A,B)**. Analysis of metastases recovered from the omentum of patients revealed IgG-positive cell clusters, suggesting that antibodies target tumor cells during the process of cancer dissemination, as well **(Supplementary Figure S1B)**. Overall, this large-scale analysis demonstrates that malignant epithelial cells are targeted by endogenous IgG antibodies in HGSOC patients.

We next examined whether IgG targeting of tumor cell surfaces occurs in other types of cancer. For this purpose, we examined 345 tumor specimens originating from 24 different human cancers derived from different organs. Quantification of IgG-coated cells using our computational analysis revealed that renal and urothelial carcinoma showed high levels of antibody coating, whereas fibrosarcoma showed nearly no fluorescence signal. B cell lymphomas were used as positive controls, since they commonly express class-switched antibodies on their surface **(Figure 1C)**. We conclude that targeting of solid tumors by IgG indicates a general phenomenon, frequently occurring in multiple cancers. Thus, in analogy to the classification of tumors as “hot” and “cold” based on immune cell infiltrates, tumors can be classified as “antibody-reactive” or “antibody-non-reactive”.

To examine if the observed antibodies physically interact with the tumor cell surface in fresh samples, the extent of IgG coating was measured by flow cytometric analysis of live tumor cells. For this purpose, fresh samples, including primary tumor, omental metastases, and cells from

ascites fluids were retrieved from surgical specimens removed from 10 stage III-IV chemo-naive HGSOC patients, followed by removal of lymphocytes and fibroblasts. The cells were incubated with fluorescent anti-IgG antibodies, and the frequency of IgG-positive tumor cells was quantified. About ~50% of the epithelial cells, including metastatic cells, were coated by IgGs on their surface, whereas the cultured control HGSOC cell line, OVCAR3, was IgG negative (**Figure 1D**). To further assess the tumor reactivity of patient-derived antibodies, we purified IgGs from ascites fluids and compared by immunofluorescence analysis their tumor binding capacity to that of IgGs purified from patient sera and age-matched healthy subjects (**Supplementary Table S2**). In this assay, 72% (18/25) of the ascites IgG samples showed tumor reactivity above the average of the controls (**Figure 1E**). These results, together with the immunohistochemistry analysis, demonstrate that the surface of tumor cells is targeted by endogenous IgGs in HGSOC patients. Next, we examined whether the tumor-reactive IgGs are produced by intratumoral ASCs. Immunohistochemistry analysis of tumor samples revealed that CD20⁺ B cells form TLS-like clusters enveloped by CD138⁺ plasma cells (PCs) scattered in the stromal tissue adjacent to the tumor cells. An average of 50% of these cells were IgG-positive ASCs (**Figure 1F**). Flow cytometry analysis revealed that 40-96.6% of intratumoral ASCs expressed IgG1 in different patients while the frequency of IgG1⁺ B cells was significantly lower (**Figure 1G**). This result demonstrates that the total B cell compartment does not represent the antibody-producing cell population. Finally, we examined if the presence of IgG⁺ ASCs or tumor binding antibodies correlates with positive patient outcomes. This analysis revealed that the presence of IgG-positive ASCs, as well as IgG-tumor coating within the cancer tissues, are associated with superior progression-free and overall survival in HGSOC patients (**Fig. 1H,I**). Collectively, our observations indicate that IgG1 is a major isotype of antibodies expressed by intratumoral ASCs with the capacity to target tumor cell surfaces.

Intratumoral antibody-secreting cells show characteristic features of antigen-driven selection

Antigen-driven positive selection and clonal expansion of B cells take place in GCs in response to immune challenge. We next examined whether the intratumoral ASCs in HGSOc are clonally related, and emerge from the antibody affinity maturation process. For this purpose, we obtained fresh tumor samples from four stage III-IV HGSOc patients who did not receive neoadjuvant chemotherapy (**Supplementary Table S3**). Single IgG1⁺ ASCs with unknown specificity were sorted from processed tumors, and their heavy (*Ighg1*) and light chains mRNAs (*Igk* and *Igl*) were sequenced by single-cell immunoglobulin sequencing (T. Tiller et al., n.d.) (**Supplementary Figure S2A**). Immunoglobulin gene analysis showed that Vh3 was the most frequent variable region in intratumoral ASCs, whereas the frequency of other specific light chain genes was more varied (**Figure 2A**). Furthermore, recurrent pairings of specific heavy and light chains were observed in individual patients, but not shared among the four patients, indicating that common public clones do not emerge in this group of patients (**Supplementary Figure S2B**). Immunoglobulin clustering based on either heavy chain or light chain sequences revealed that in each of the four patients, at least 44.4% of the sequences were recovered more than once, suggesting that ASCs in tumors were clonally expanded. Heavy chain analysis revealed 11-36 expanded clonotypes per patient, comprising 44.4-78.38% of the ASCs obtained from each of the four patients, including a single dominant clone, with a frequency ranging between 5.85-18% of the total sequences (**Figure 2B, C**). Similar results were obtained following a more precise analysis using coupled heavy and light chain sequences for definition of a clone (**Figure 2C**). The ASC

immunoglobulin genes displayed a level of SHMs that is typical of circulating memory cells, with averages ranging between 17.29-21.69 mutations per heavy chain and 10.3-16.46 mutations per light chain (**Figure 2D**). These paired measurements correlated closely on a single cell basis for all of the patients, and accordingly validates our immunoglobulin sequence analyses (**Supplementary Figure S2C**). To examine whether the intratumoral ASC clonal members were produced through clonal diversification, we reconstructed lineage trees of clones recovered from tumors using PHYLIP and Alakazam (Felsenstein 2005; Gupta et al. 2015). We found several families of clones that exhibited clonal diversification by progressive SHM accumulation, indicating that these cells are the product of stepwise positive selection (**Figure 2E**, **Supplementary Figure S3**). We conclude that significant numbers of ASCs in the tumor microenvironment diversified by SHMs from a common ancestor, suggesting that their clonal expansion was driven by specific antigens as part of a T cell-dependent immune response.

MMP14 is a major antibody target in HGSOC patients

To further study the nature of the humoral immune response in HGSOC patients, we cloned the immunoglobulins that we isolated, and expressed them as monoclonal antibodies (**Supplementary Table S4**). To this end, immunoglobulins representing expanded clones were primarily selected for antibody production. Within each clonal family, either immunoglobulin sequences that represent multiple clonal members or clones with the highest SHM load were chosen (**Supplementary Figure S3**). In order to examine whether the monoclonal antibodies bind patient-derived tumor cells, we established HGSOC primary cultures originating from the primary tumor, omental metastasis, and ascites-derived tumor cells of three different patients. To remove cell-bound antibodies, as well as fibroblasts and immune cells, the tumor cells were isolated, cultured

and maintained for 2-3 passages. Flow cytometry analysis showed that all of the cultured cells were EpCAM positive (**Supplementary Figure S4A**). Monoclonal and secondary antibodies were incubated with monolayers of primary tumor cultures or with the OVCAR3 cell line followed by measurement of the fluorescence signal. To avoid biases that can potentially arise from the different numbers of cells per sample, we also stained the monolayers with DAPI, which allowed us to normalize the fluorescence signal to the number of cells in each replicate. This analysis revealed that all the patients produced tumor-binding antibodies. Out of 27 monoclonal antibodies, 15 bound the primary and ascites-derived tumor cultures, and 17 of the monoclonal antibodies interacted with the cells that were generated from the omental metastasis tumor cells (**Figure 3A**). To provide direct evidence for tumor cell binding by monoclonal antibodies, we stained OVCAR3 monolayers and measured antibody binding on the single cell level by fluorescence microscopy and QuPath analysis (**Supplementary Figure S1**). This approach revealed that most of the antibodies bound directly to the tumor cell lines (**Figure 3B**). Furthermore, the monoclonal antibodies primarily interacted with ovarian carcinoma cell lines (OVCAR3 and 4) and a pancreatic cancer cell line (PANC1), and to a lesser extent with cells derived from other organs, suggesting specificity to both ovarian and pancreatic tumors, presumably through shared surface target antigens (**Supplementary Figure S4B**). Thus, the ASCs located within the tumor microenvironment produce tumor-targeting antibodies.

Ovarian and pancreatic cancers are highly desmoplastic (fibrotic) and are constantly subjected to remodeling of their microenvironments by matrix proteases (Kamel et al. 2010; Cathcart et al. 2016; Maria Caroline Vos et al. 2016; Sakata et al. 2000). The ECM-remodeling enzymes, MMPs, were previously demonstrated to trigger the generation of autoreactive antibodies in autoimmune diseases and viral infection, suggesting that they may also provoke an immune response in cancer (Crowley et al. 2016; Nishijima et al. 2004; Sato et al. 2003; Wang et al. 2020). Furthermore, it

was suggested that high levels of antigen can lead to a break of tolerance and generation of autoantibodies in cancer (Kamel et al. 2010; Cathcart et al. 2016; Maria Caroline Vos et al. 2016; Sakata et al. 2000). Therefore, we evaluated the binding capacity of polyclonal IgGs derived from ascites fluids from 25 patients (**Supplementary Table S2**) to 6 recombinant MMPs, and an additional 3 ECM-associated targets. In this setting, BSA was used as a negative control antigen, and p53, which elicits an antibody response in HGSOC (Anderson et al. 2015), was used as a positive control target. ELISA revealed strong and reproducible antibody reactivity against MMP14 in all of the patients, whereas reactivity to other MMPs was also evident, but to a lesser extent (**Figure 3C**). Accordingly, analysis of HGSOC RNA-seq data sets showed high expression of MMP14 compared to other expressed genes, as well as in comparison to healthy control tissues (**Supplementary Figure S5A, B**). Immunohistochemistry analyses revealed strong expression of MMP14 on cancer cells, whereas adjacent healthy tissues showed lower expression levels (**Supplementary Figure S5C**). Furthermore, using western blot analysis, MMP14 protein expression was also detected in tumor cell lines as well as in patient-derived tumors (**Supplementary Figure S5D**). Thus, since MMP14 is highly expressed on tumors, and since ascites-derived antibodies show high reactivity with this enzyme, we reasoned that this is a highly relevant target in HGSOC patients for further testing of patient-derived monoclonal antibodies. Evaluation of monoclonal antibody binding to MMPs by ELISA revealed several immunoglobulins that reproducibly bound to MMP14, with mild to moderate cross-reactivity with other MMP enzymes (**Figure 3D**). Strikingly, in all 4 of the patients, monoclonal antibodies that bound MMP14 with various degrees of efficacy and specificity were detected, confirming our analyses using polyclonal patient-derived antibodies. To strengthen our findings, we tested the binding of monoclonal antibodies to MMP14 at different dilutions by ELISA, and found a dose-dependent response (**Figure 3E**). To examine if these antibodies are reactive with many types of

antigens (polyreactive) we tested their binding to a panel of structurally unrelated, biologically relevant antigens, including insulin, double-stranded DNA, and lipopolysaccharide by ELISA. Typically, antibodies that bind at least two members of this defined set of antigens are considered polyreactive (Wardemann et al. 2003). ED38, a well-characterized polyreactive antibody was used as a positive control, and GD01, an antibody that binds an unrelated target (Junin virus GP1) was used as a negative control. Minimal binding of the monoclonal antibodies to the unrelated targets was detected even at high antibody concentrations, whereas the polyreactive ED38 was strongly positive in this assay (**Figure 3F**). Similar results were obtained by testing binding to human epithelial type 2 (HEp-2) cell lysates, a commonly used assay to determine antibody polyreactivity (**Figure 3F**). We conclude that the monoclonal antibodies that we isolated are not polyreactive and show strong binding to MMPs and in particular MMP14, which is abundantly expressed on the surface of HGSOC tumor cells.

Our findings indicate that self-reactive antibodies are formed in cancer patients with the potential to bind healthy tissues in addition to tumor cells. To examine this possibility, we purified IgGs from serum and ascites of individual patients and examined their binding capacity to several normal tissues including fallopian tube, uterus, pancreas and colon tissues, all of which are known to express MMP14. Staining with LEM 2/15, a well-characterized mouse antibody that binds MMP14 (Udi et al. 2013), confirmed MMP14 expression on various cell types within the healthy tissues (**Supplementary Figure 6A**). This analysis revealed that antibodies derived from patient serum can bind healthy tissues, though, significantly less effectively than ascites-derived antibodies. To evaluate whether self-reactive antibodies persist during cancer remission, we collected blood from eight patients who completed their adjuvant treatment. All patients evaluated exhibited CA125 values within the normal range, and no evidence of disease was observed by PET-CT (**Supplementary Table S5**). ELISA revealed a weak signal in this cohort which was

above the background which was detected in healthy controls and only one out of the eight patients had high levels of anti-MMP14 antibodies in her serum (**Supplementary Figure S6B,C**).

Finally, a large-scale retrospective analysis of 870,356 women (including 3,353 ovarian cancer patients) over a follow-up period of up to 15 years was performed based on the electronic health record (EHR) database from Clalit Healthcare Services (Balicer and Afek 2017). This analysis did not reveal an increased incidence of autoimmune diseases among patients previously diagnosed with ovarian cancer (**Supplementary Figure S6D**). Collectively, although we did find autoantibodies in sera of HGSOc patients, no signs of autoimmune diseases were detected in the patients. Of note, the recovered patients were subjected to various treatments, including chemotherapy, which may affect their ability to produce antibodies.

Characterization of a patient-derived monoclonal antibody that binds MMP14

To provide additional evidence for MMP14 binding by patient-derived antibodies, we further characterized one such clone, T13, an antibody that showed effective binding to MMP14 by ELISA in multiple antigen binding assays. Using the Octet QKe platform, we found that the K_d value of T13 was $410 \pm 45 \text{ nM}$ ($R^2 = 99.34\%$) (**Figure 4A**). To examine whether T13 binds a linear epitope or a complex protein conformation, we performed a western blot analysis on 14 different cell lines of epithelial, mesenchymal and neural crest origin, representing a wide variety of cell types and organs. Bands of approximately 63 kDa were detected in this assay, compatible with the size of MMP14, and an additional $\sim 35 \text{ kDa}$ band appeared as well, which coincides with a known degradation product of MMP14 (**Figure 4B**). Notably, OVCAR3 and HT1080, which express high levels of MMP14, showed the strongest signals and very few additional bands were detected. To verify that the antibody binds native MMP14, we expressed MMP14 together with mCherry in K562 cells. Whereas the antibody did not show binding to mCherry-negative cells, mCherry-

positive cells showed clear antibody binding by flow cytometric analysis (**Figure 4C, and Supplementary Figure S4C**). To further examine cross-reactivity and to identify additional potential surface targets, we tested the binding of T13 as well as an antibody that did not bind OVCAR3 as a control (T15) to a microarray that included 9400 recombinant human proteins (either full length or fragments). Although several membrane proteins showed reactivity with T13, manual inspection of their sequences and validation by traditional ELISA did not reveal additional surface molecules that could serve as a target for the monoclonal antibodies on tumor cells (**Supplementary Fig. S7A,B and Supplementary Table S6**). Other antibodies that were tested in this assay did not reveal cell surface or tumor-associated targets that are relevant to HGSOC. Overall, these results demonstrate that a linear epitope on MMP14 is a major target for the T13 monoclonal antibody.

To identify the binding site of T13 on MMP14, we used a phage display assay to analyze binding to random peptides (Ashkenazy et al. 2021; Freund, Enshell-Seijffers, and Gershoni 2009). Whereas an antibody that did not show tumor-reactivity (T15) interacted with only 10,222 peptides, T13 interacted with 529,495 peptides and 85.1% of these showed a strong homology to a sequence found in the MMP14 catalytic site (**Figure 4D**). ELISA confirmed binding of T13 and of T12, an additional clonal member with similar specificity, to the homologous sequence found on MMP14 but not to a control peptide derived from a non-binding region (**Figure 4E**). Further to this analysis, the molecular structure of the T13 antibody was modeled using the AlphaFold framework (Mirdita et al. 2021; Jumper et al. 2021) followed by Global Docking computation of the MMP14-T13 atomic model complex. The PatchDock algorithm was used to dock the MMP14 (PDB 5H0U) atomic model to the predicted T13 model using the protein-protein refinement stage on the FireDock server (Duhovny, Nussinov, and Wolfson, n.d.; Schneidman-Duhovny et al. 2005; Andrusier, Nussinov, and Wolfson 2007; Mashiach et al. 2008). This analysis resulted in a “top

hit” comprising the peptide sequence found in our phage display assay and identified by ELISA. Collectively, these data predict the binding epitope of one of the patient-derived antibodies on MMP14.

Acquisition of somatic hypermutations contributes to antibody tumor-reactivity

B cell central tolerance is established during development of mature B cells in the bone marrow (BM) where autoreactive clones are eliminated. Nonetheless, it has been estimated that 5% of the B cells that emerge from this process are autoreactive, but typically do not cause an apparent autoimmune disease (Wardemann et al. 2003). An additional pathway for the generation of autoreactive antibodies is through insertion of SHM into immunoglobulin genes of antibodies that do not bind a self target in their original germline version (Piccoli et al. 2015; Di Zenzo et al. 2012; Mietzner et al. 2008; Schroeder, Herrmann, and Winkler 2013; Thomas Tiller et al. 2007). To examine whether the binding of patient-derived monoclonal antibodies depended on SHMs for tumor binding, we generated parental immunoglobulin configurations by reverting their sequence to their germline versions and tested their binding capacity to OVCAR3 using fluorescence

microscopy and QuPath analysis. For this purpose, we used antibodies that showed significant or moderate tumor binding by the immunofluorescence assay (**Figure 4A**). This assay revealed eleven patient-derived monoclonal antibodies that lost tumor binding after removal of SHMs, and an additional twelve antibodies that did not show a significant decrease in tumor binding in their germline form (**Figure 5A**). Interestingly, two antibodies gained binding to the tumor cell line after removal of the SHMs (**Figure 5A**). We conclude that two types of tumor-reactive antibodies exist in the patients, one that depends on SHM for tumor binding (Class I), and another type that binds the tumor in their germline form (Class II).

To strengthen our antibody classification, we tested binding of germline antibodies to MMP14 using dilution ELISA. Similar to the previous experiment, this analysis revealed two groups of antibodies, one that depends on SHMs for MMP14 binding, and one whose members bind MMP14 in their germline configurations (**Figure 5B**). These data suggest that anti-tumor antibodies can form before introduction of antigen in a germline version, and also develop through the acquisition of SHMs.

To gain more insight regarding the role of SHMs in affinity maturation, in addition to the germline configuration, we generated inferred ancestors based on shared and non-shared SHM among sequences within clonal families. For this purpose, sequences that contain only shared mutations in their downstream diversified progenies were used for generation of monoclonal antibodies. ELISA demonstrated that T13 shows effective binding to MMP14, whereas its inferred ancestor exhibited decreased binding when the non-shared mutations of its progenitor were removed in a stepwise manner (**Figure 5C**). Similar results were obtained by analysis of the inferred ancestors of T17 (**Figure 5C**). These two examples indicate that a stepwise increase in affinity against MMP14 may occur in HGSOC patients.

Patient-derived autoantibodies support antibody-mediated effector functions

To examine whether the two antibody classes exhibit potential antitumor effector activity, we examined their Fc-mediated functions. Antibodies can support antibody-dependent cellular phagocytic (ADCP) activity through interaction with Fc receptors expressed on phagocytic cells (Wieland and Ahmed 2019; DiLillo and Ravetch 2015; Webb, Bernshtein, and Alter 2021). Incubation of THP-1 monocytes with 25 patient-derived polyclonal antibodies (**Supplementary Table S2**) and MMP14-coated beads induced their effective uptake by the cells (**Figure 6A**). Furthermore, incubation of polyclonal antibodies with OVCAR3 cells induced antibody-dependent cell cytotoxicity (ADCC) by NK cells (**Figure 6B**). Of note, these antibodies carry post-translational modifications which were introduced naturally within the patients. In contrast, only some of the monoclonal antibodies were effective in inducing effective ADCP and ADCC (**Figure 6C, D**) suggesting different affinities and targeted epitopes affect the functions of specific antibodies. These results demonstrate that all of the ovarian cancer patients have antibodies with effector function potential, but not all of the antibodies are able to trigger anti-tumor activity by effector cells. Nonetheless, whereas clusters of T cells were detected in the stromal compartment of most of the HGSOC tumors, NK cells were very rare (**Supplementary Figure S7C**). Collectively, these findings indicate that tumor-reactive antibodies in HGSOC have functional potential. Yet, ineffective recruitment of effector cells, such as NK cells, into the tumors, or dysfunction of other cell types (DeNardo and Ruffell 2019), may preclude effective activation of cell-mediated antibody-effector functions.

Discussion

The presence of B cells in tumors was associated with a positive prognosis in some cancers, yet it remains unknown how tumor-binding antibodies evolve. Using large-scale imaging approaches, we demonstrate that the surface of HGSOC and many other tumors are frequently coated with endogenous IgG antibodies. Through bait-free single-cell sequencing and antibody cloning, we found that SHMs support endogenous antibody-mediated immune response in HGSOC patients in parallel to pre-existing antibody autoreactivity. Conceptually, our results describe the evolution of the serological immune response in cancer patients, and show that antibodies that bind the tumor cells can emerge from non-reactive precursors through antigen-driven positive selection (Class I). In parallel, pre-existing autoreactive B cells that escape deletion during negative selection in the bone marrow are also recruited to the tumor and contribute to the overall humoral immune response (Class II). As opposed to autoantibodies in deleterious autoimmune diseases, both antibody classes have the potential for beneficial functions in cancer patients; however, additional players are required for effective tumor eradication, such as infiltration of effector cells.

It was shown that a humoral immune response against foreign viral proteins can form in HPV-driven head and neck cancer (Wieland et al. 2020). We demonstrate that autoantibodies against self-antigens are formed in HGSOC patients, but in contrast to the immune response elicited against foreign antigens, this process must involve a break in immune tolerance. It is most likely

that the unusually high levels of antigens, such as MMP14, activate rare autoreactive B cells with the capacity to generate autoantibodies (Kaimal et al. 2013; Zaenker, Gray, and Ziman 2016). This hypothesis is difficult to test in human patients, since the antibodies represent the end product of the immune response, when the break in tolerance already occurred. We suggest that the chronic nature of the cancer and high antigenic load has the potential to drive the accumulation of SHM over time, and generate endogenous antibodies with a tumor-binding capacity.

MMP14 is highly expressed in HGSOC and activity of this enzyme is essential for tumor progression and metastatic dissemination (Kaimal et al. 2013; M. Caroline Vos et al. 2021; Moss et al. 2009). We recovered several tumor-binding antibodies, of which 9 showed reactivity with MMP14, as well as milder cross-reactivity with other similar enzymes but not with other protein and non-protein targets that were tested. Since MMP14 is a surface-bound enzyme and expressed in unusually high levels on the tumor surface, we suggest that this is the most relevant self-target of our cloned antibodies in HGSOC. Nonetheless, we cannot rule out the possibility that other antigens are targeted by MMP14-reactive antibodies, as well.

The presence of SHM and gradual increase in antibody affinity from the germline configuration to the final mutated form indicates that an antigen-driven process took place in the patients. Acquisition of SHMs typically takes place in GCs that can be either located in the tumor within TLS, or in tumor-draining lymph nodes (Kroeger, Milne, and Nelson 2016). Of note, the size of excised ovarian tumors is large, typically ranging from 5 to more than 30 cm in their largest dimension. In order to extract and sequence antibody-secreting cells, we used a very small fragment of the tumor (less than 1 cubic cm). If cells clonally expand at a distant site and then home to the tumor through the circulation, the chances of detection of clonally related ASCs without a bait is extremely small, as they would be expected to spread throughout the tumor tissue and other organs such as the BM and mix with other non-related clones. Yet, the possibility that

the mutated cells originated from draining lymph nodes cannot be excluded, and further studies are needed to address this question.

Affinity-based selection is a highly regulated process that involves well defined cellular and molecular interactions (Biram, Davidzohn, and Shulman 2019). Nonetheless, it remains possible that the response started as a “bystander” reaction and drifted towards MMP14 specificity, as a result of the abundant antigen or a different break-of-tolerance driver. Indeed, few autoreactive cells have the potential to generate new self-reactive antibodies through epitope spreading, and thereby enhance the overall autoreactivity against the tumor (Degn et al. 2017; Vinuesa, Sanz, and Cook 2009; Cornaby et al. 2015). An additional possible source of Class I antibodies are mutated memory cells that evolved in response to foreign stimuli, and acquire cross-reactivity with tumor antigens, as demonstrated in some infectious diseases (Yang et al. 2021). As opposed to Class I, the Class II antibodies are tumor-reactive, and yet SHMs did not contribute to their tumor binding capacity, which might suggest that they were elicited against a different antigen, while retaining their original reactivity towards MMP14. Thus, it is most likely that Class II antibodies emerged in a bystander response, which was further amplified in response to the tumor cells. Furthermore, since the B cell response is ongoing within the patients, Class II antibodies can potentially convert to Class I upon acquisition of additional SHMs.

Our work demonstrates that, in contrast to cell-mediated immune responses, the humoral response against the tumor in HGSOC is largely intact and has the potential to trigger Fc-mediated anti-tumor effector functions (Webb, Bernshtein, and Alter 2021). Yet, it was shown that antibodies can interact with Fcγ receptors on tumor-associated macrophages, promoting angiogenesis and tumor progression (Andreu et al. 2010; DeNardo and Ruffell 2019). Furthermore, in this context it was demonstrated that inhibition of Fcγ receptor signaling can reverse the T cell dysfunctional state in tumors, suggesting that macrophage engagement with antibodies could have an

immunosuppressive effect on the anti-tumor immune response (DeNardo and Ruffell 2019). It is most likely that dysfunctional phagocytic cells and insufficient recruitment of effector cells such as NK cells preclude adequate antibody-mediated effector functions such as ADCP and ADCC (Uppendahl et al. 2017). Nonetheless, the presence of IgGs and other isotypes in the tumor correlated with disease-free progression and patient survival, suggesting that antibodies in patients have overall beneficial functions (Biswas et al. 2021; Hu et al. 2019).

Collectively, our study describes a target for antibodies in HGSOV, and demonstrates that the responding antibodies are divided into two classes, based on their origin. Patient-derived monoclonal antibodies are potentially useful for chemoattractant or drug delivery to tumors and for cell-mediated therapeutic approaches, such as in CAR-T cell therapy.

Limitations of the study

Since we examined samples from human patients rather than a mouse lab model, we were unable to explore the mechanism through which the break of tolerance occurred in the patients, and further studies should address this point. Furthermore, while we found that several of the monoclonal antibodies bind MMP14, we cannot exclude additional targets, as well. Lastly, since we examined antibody-forming cells isolated from the tumors, we were unable to determine if they originated from the tumor mass or migrated from tumor-draining lymph nodes.

Acknowledgments: Z.S. is supported by the Morris Kahn Institute for Human Immunology, Human Frontiers of Science Program (CDA-00023/2016), Azrieli Foundation, The Moross Integrated Cancer Center, Rising Tide Foundation, Israel Science Foundation (1090/18). This study was also supported by RCDA (18-703-R) and Beverley Lubrach Abshez initiative for ovarian and female reproductive system cancers (Israel Cancer Research Fund), Ben B. and Joyce E. Eisenberg Foundation, Wolfson Family Charitable Trust & Wolfson Foundation, Elie

Hirschfeld and Dr. Sarah Schlesinger and Miel de Botton. Z.S. is a member of the European Molecular Biology Organization (EMBO) Young Investigator Program. I.S. is an incumbent of the Maurizio Pontecorvo Professorial Chair and has received funding from the European Union's Horizon 2020 research and innovation program (grant agreement No 801126), European Research Council (ERC) under the European Union's Horizon 2020 research and innovation program (grant agreement No 695437), Israel Science Foundation (1800/19), and The Thompson Family Foundation. M.D.S. is supported by Marie Skłodowska-Curie Individual Fellowship (Horizon 2020 Grant No. GAP-845066).

Author Contributions:

R.D.M conceived the study, designed, and conducted the experiments, performed data analysis, and wrote the manuscript. N.N conducted antibody cloning and expression and the ADCP experiments. A.G performed the immunoglobulin repertoire and clonality analyses, L.S.B assisted in cell sorting and manuscript preparation. I. Solomonv supervised biochemical analyses, A.H. generated and characterized recombinant proteins, L.M performed in-silico docking. Y.D assisted in immunofluorescence staining. M.D.V conducted the protein array antigen screens. H.H conducted bioinformatic analyses of gene expression databases. I.Z performed some of the BCR sequencing. M.M performed the phage display assays. O.G helped developing the QuPath analysis, G.S, A.J.S, L.S, and E.Y recruited patients, performed the surgical procedures and provided clinical information. E.R supervised and performed the clinical procedures, patient recruitment and provided important clinical insights. N.Y and M.F performed the pathological evaluation of the samples. D.T, I.E and E.P participated in recruiting patients, collecting samples and establishing the clinical database. N.M.C performed the analyses based on the Clalit healthcare services EHR database. J.M.G, generated the phage display assay. N.F supervised the phage display experiment. Y.M supervised the protein array antigen screens. G.Y supervised the immunoglobulin sequence analyses. I. Sagi supervised the study, designed experiments, and wrote the manuscript. Z. S. conceived the study, supervised the study, designed experiments, and wrote the manuscript. All authors discussed the results and contributed to the final manuscript.

Declaration of interests

The antibodies reported in the article are in the process of being patented.

Figure Legends

Figure 1. Tumor-reactive antibodies and IgG⁺ ASCs are frequently detected in solid tumors.

(A, B) H&E and anti-human IgG staining (A), and quantification (B) of archival FFPE samples derived from chemo-naïve HGSOC patients (**Supplementary Table S1**) and healthy tissues of the female reproductive tract. IgG⁺ and IgG⁻ tumor cells are represented in red and purple, respectively. IgG⁺ and IgG⁻ stromal cells are shown in light and dark green, respectively. Scale bars, 100µm. **(C)** Quantification of IgG coating on 24 human cancer types. Black lines represent the interquartile range. Below, representative examples of four tumors. Scale, 100µm. **(D)** Flow cytometric analysis of fresh tumor cells retrieved from stage III-IV chemo-naïve HGSOC patients and stained with anti-IgG. OVCAR3 cell line cells were used as negative control. Each dot represents the fraction of IgG⁺ tumor cells in an individual patient. **(E)** Immunofluorescence staining of OVCAR3 cells using purified IgGs (500nM) from ascites fluids and sera of HGSOC patients and healthy controls (**Supplementary Table S2**). Quantification of fluorescence normalized to DAPI staining is shown. Scale, 40µm. Each dot represents IgGs from individual patients. **(F)** CD20, CD138, IgG and DAPI staining of HGSOC tumor slides. Lower left image scale, 50µm, lower right image scale, 20µm. **(G)** Flow cytometric analysis of HGSOC intratumoral IgG1⁺ B cells and ASCs. **(H, I)** Association between the presence of IgG⁺ ASC (H), and tumor-reactive IgG (I) with progression free and overall survival in HGSOC patients. Quantification of ASCs was averaged from 3 different high power fields. In B, P values were determined by two-tailed Student's t test. In D, statistical significance was determined by one way analysis of variance (ANOVA) followed by Dunnett's post-hoc test. In E, the Kruskal-Wallis test was used followed by Dunn's post-hoc test. In G, P values were determined by two-tailed Student's paired t test. In

H and I statistical significance between curves was determined using the log-rank (Mantel-Cox) test.

Figure 2. Antibody secreting cells in the tumor microenvironment are clonally related. (A) Immunoglobulin analysis of intratumoral CD38⁺⁺ IgG1⁺ ASCs derived from the primary tumors of four HGSOC patients. Pie charts depicting the relative abundance of V (variable) genes. **(B)** The fraction of expanded clones out of total immunoglobulin sequences. **(C)** The frequency of clonal families out of the total sequenced clonotypes of *Ighg1* or *Ighg1* and light chain sequences. Each colored slice represents a unique ASC clone. White slices represent unique clonotypes. The total number of analyzed immunoglobulins is shown in the center. **(D)** Number of mutations per antibody chain (V and J segments). **(E)** Examples of phylogenies of expanded intratumoral ASC clones based on paired sequences. Gray circles represent the hypothetical germline configuration. White circles represent hypothetical ancestors. Pale colored circles represent immunoglobulins identified by heavy chain sequences only. Bold colored circles represent immunoglobulins identified by both heavy and light chain sequences. Dotted arrows represent a Hamming distance of >15 nucleotides. Numbers appearing above arrows represent the number of distinct heavy chain mutations accumulated between clonal members. Each color represents an individual patient.

Figure 3. Tumor-reactive MMP14 autoantibodies are generated in HGSOC patients. (A) Representative images and quantification of normalized MFI of primary cultured tumors or OVCAR3 cells stained with monoclonal antibodies (500nM) and DAPI. The IgG fluorescent signal was normalized to DAPI to account for potential variability in cellular density between replicates. Each color represents an individual patient. Bars represent mean values of 2-3 replicates, whiskers represent standard deviations. **(B)** Representative images and quantification of the mean fluorescence intensity of OVCAR3 cells stained with different monoclonal antibodies

(500nM). Quantification of MFI was performed on each cell separately using QuPath v0.2.0-m9. Boxes are divided by the median value and represent the interquartile range, whiskers represent the 10-90 percentiles. The dashed line represents mean background fluorescence. Scales, 50µm. Each color represents an individual patient. **(C, D)** Analysis of patient-derived polyclonal (C), and monoclonal (D) antibody binding to the indicated targets by ELISA. The heatmap depicts the mean optical density data from two independent ELISA. All antibodies were screened at a concentration of 100nM. **(E)** ELISA showing dose-dependent binding of monoclonal antibodies to MMP14. **(F)** ELISA of monoclonal antibodies against structurally distinct targets and the HEp-2 cell line lysate. ED38 was used as a positive control and the GD01 antibody as a negative control. In A, comparison between the test antibodies and the isotype control was performed using one way ANOVA followed by Dunnett's post-hoc test. In B, comparison to the isotype control was performed using the Kruskal-Wallis test followed by Dunn's post-hoc test.

Figure 4. T13 monoclonal antibody binds a linear epitope on MMP14. **(A)** Measurement of the kinetic constants governing the binding of the T13 mAb to MMP14 by biolayer interferometry analysis using the Octet QKe platform. **(B)** Western blot analysis of T13 binding to various cell line lysates. **(C)** Analysis of T13 binding to K562 cells over-expressing MMP14:mCherry. Fluorescence intensity values from three independent experiments are shown. **(D)** Phage display data depicting the epitope sequence of mAb T13 in the catalytic domain of MMP14. The X axis represents the amino acid sequence (108-293) of MMP14 catalytic domain. The bars represent the number of NGS reads of different peptides that were aligned to a given amino acid sequence. Bar colors are coded to the top 25 enriched peptides whose relative abundance is depicted in the pie chart. The number of NGS reads per peptide represents the average of three replicates. **(E)** ELISA using the putative epitope of T13 and a control peptide, and mAbs T13 and T12. The dashed line

represents an FMO control. **(F)** In silico structural representation of T13-V_HV_L antibody targeting the predicted binding epitope on MMP14. The antibody framework appears in light purple, CDRs in cyan; MMP14 marked in green with the phage-display epitope in blue. In C, one way ANOVA was used followed by Dunnett's post-hoc test.

Figure 5. Tumor-reactive antibodies arise from autoreactive and non-binding precursors.

(A) Quantification of OVCAR3 binding by mutated and non-mutated antibodies (500nM) as measured by fluorescence microscopy. Quantification of mean fluorescence intensity was performed on each cell separately using QuPath v0.2.0-m9. Boxes are divided by the median value and represent the interquartile range; whiskers represent the 10-90 percentiles. Fold change in median fluorescence of the mutated antibody compared to the non-mutated putative ancestor is indicated. **(B)** ELISA for MMP14 binding using mutated and non-mutated monoclonal antibodies. **(C)** ELISA for MMP14 using T3, T17, their inferred ancestors, and their germline configurations. In A, a comparison between the mutated version and germline configuration of each antibody was performed using the Mann-Whitney U test. A difference in medians was found to be statistically significant in all panels with a $p < 0.0001$, except mAb T18 ($p < 0.01$) and mAb T23 (ns).

Figure 6. Patient-derived and monoclonal antibodies support effector functions.

(A) Flow cytometric quantification of patient-derived polyclonal antibody mediated phagocytosis of MMP14-coated beads by THP-1 monocytes. Polyclonal antibodies were introduced at a concentration of 1 μ M. **(B)** Longitudinal quantification of antibody dependent cell-mediated cytotoxicity (ADCC) targeting OVCAR3 cells, in the presence of NK cells alone, and together with patient-derived polyclonal antibodies (500nM). A commercial anti-EGFR antibody (Cetuximab) was used as positive control. **(C)** Phagocytosis analysis as in A using monoclonal

antibodies (500nM). GD01 was used as a negative control. **(D)** OVCAR3 killing by NK cells in the presence of monoclonal antibodies (500nM). An average of four reactions with standard deviation is shown. In A-D, statistical significance was determined by one way ANOVA followed by Dunnett's post-hoc test.

Supplemental figure titles and legends

Figure S1. Machine learning methodology for identification of different cellular populations and measurement of IgG coating in large tumor specimens. Related to Figure 1. (A) The top panel depicts a typical tumor specimen at low (top) and high (bottom) magnifications. Corresponding scale bars are 2mm and 100 μ m, respectively. Tumor and healthy control slides stained with anti-IgG and DAPI were scanned and analyzed using the QuPath v0.2.0-m9 software. Nuclei in the specimens were detected on the basis of the DAPI data and the cellular border was extrapolated at a distance of 2 μ m from the nuclear border. An object classifier was trained to identify tumor cells versus non-transformed cells on the basis of multiple morphologic features. Following annotation, the IgG mean fluorescence intensity was measured for each individual cell in the area surrounding the nucleus. IgG⁺ and IgG⁻ tumor cells are annotated in red and purple respectively, IgG⁺ and IgG⁻ non-tumor cells are annotated in dark green and light green, respectively, and the frequency of IgG positive tumor cells or healthy epithelial counterparts is quantified for each specimen. The bottom panel demonstrates an example of the method described above (scale, 4 μ m) at the single cell level. Note that while stromal and immune cells may stain positive for IgG, they were excluded from the tumor cell quantification based on their distinct morphological characteristics. **(B)** Heterogeneous IgG staining in two adjacent tumor nests derived from an HGSOC omental metastasis from a single patient. Scales, 100 μ m.

Figure S2. Light and heavy chain pairing analyses. Related to Figure 2. (A) Schematic representation of single cell ASC sorting, immunoglobulin sequencing, cloning and antibody expression pipeline. (B) Circos plots linking coupled heavy and light chain sequences in all four patients according to their V alleles. The left plot represents paired expanded clonotypes in all four patients. The right plots represent all paired clonotypes in each patient. Heavy chain V_H alleles are represented in the lower circos arcs and light chain V_K alleles are represented in the upper arcs. Band widths represent the incidence of a given $V_H:V_K$ combination. (C) Correlation between the mutational load in the heavy and light immunoglobulin chains per patient. The degree of correlation was calculated using Pearson's correlation coefficient. Line represents a linear regression model, dotted lines represent the error range.

Figure S3. Schematic representations of expanded intratumoral ASC clones. Related to Figure 2. Additional examples of phylogenies of expanded intratumoral ASC clones based on paired sequences. Gray circles represent the hypothetical germline configuration. White circles represent hypothetical ancestors. Pale colored circles represent immunoglobulins identified by heavy chain sequences only. Bold colored circles represent immunoglobulins identified by both heavy and light chains. Dotted arrows represent a Hamming distance of >15 nucleotides. Numbers appearing above the arrows represent the number of distinct heavy chain mutations accumulated between clonal members. Annotated circles represent monoclonal antibodies which were cloned and expressed.

Figure S4. Tumor-derived antibodies interact preferentially with ovarian carcinoma cell lines. Related to Figure 3. (A) Flow cytometric analysis confirming the expression of the epithelial cell marker EpCAM in three primary cultures derived from primary tumor, omental

metastasis and ascites fluids of three different HGSOC patients, as well as in the OVCAR3 cell line as a positive control and PBMCs as a negative control. **(B)** Fluorescence analysis for binding of monoclonal antibodies to various cell lines. The fluorescence intensity was normalized to DAPI staining. GD01 was used as a negative control. **(C)** Flow cytometric analysis confirming successful transfection of K562 cells with the *mmp14*:mCherry construct.

Figure S5. MMP14 is highly expressed in HGSOC. Related to Figure 3. **(A)** Correlation matrix depicting the mean expression level of genes derived from published RNA sequencing data sets of 85 HGSOC primary tumors (GSE102094) and 35 HGSOC omental metastases (GSE71340). Each dot represents a mean Log₂CPM value. Specific gene families are highlighted – MMPs in red, ADAMs in purple, LOXs in green, Kallikreins in yellow, and house-keeping genes in blue. The yellow, orange and pink backgrounds represent RNA corresponding to the top 10%, 5% and 1% genes, respectively. The dashed circle represents the most highly expressed matrix degrading enzymes in both the primary tumor and metastasis. **(B)** Normalized MMP14 expression levels and standard deviations in a published RNA sequencing dataset of 85 HGSOC primary tumors and pools of normal ovary and fallopian tube tissues (GSE102094). **(C)** MMP14 immunofluorescence staining and quantification originating from 32 FFPE specimens derived from 26 HGSOC primary tumors and 6 metastases adjacent to healthy marginal tissues. MMP14 staining intensity was measured on the single cell level in various diseased and healthy cellular compartments and quantified using the QuPath v0.2.0-m9 software. Scale bars, 50µm. In each graph tumor cells to an adjacent normal tissue are compared. **(D)** Western blot analysis for MMP14, performed on lysates from different cell lines and patient tumor samples. In A, the degree of correlation was calculated using Pearson's correlation coefficient. The black line represents a linear regression model. In B, *P* values were calculated by DESeq2. In C, *P* values were determined by two-tailed Student's paired t test for matched samples.

Figure S6. Serum derived antibodies in HGSOC patients are reactive with healthy MMP14 expressing tissues. Related to Figure 3. (A) Upper panel: Dual immunofluorescence staining of consecutive tissue sections derived from a healthy fallopian tube. Staining was performed with the commercial anti-MMP14 antibody LEM-2/15.8 and polyclonal antibodies (500nM) derived from patients or healthy control individuals. Polyclonal IgGs originated from 3 healthy controls as well as from matched sera and ascites samples acquired from 7 HGSOC patients. The ascites fluids and serum samples were taken from the patients at the same time. Lower panel: Quantification of ascites or sera IgG staining of MMP14 expressing epithelial compartments on various healthy tissues. Healthy tissues evaluated included the fallopian tube, endometrial uterine lining, pancreas and colon. In these specimens, MMP14 expressing epithelial compartments were defined using QuPath v0.2.0-m9 on the basis of LEM-2/15.8 staining. IgG staining was quantified per cell and normalized to the background signal. Scale bar: 20 μ m **(B)** ELISA comparing the MMP14 reactivity of control sera to that of ascites-derived polyclonal and anti MMP14 monoclonal antibodies. **(C)** ELISA comparing the MMP14 reactivity of sera from HGSOC patients in remission to that of an anti MMP14 monoclonal antibody. **(D)** Annual incidence rate of autoimmunity among women who were previously diagnosed with ovarian cancer compared to female controls following adjustment to age and calendar year. Bars represent the annual incidence rate of autoimmunity per 100,000 women. Whiskers represent the confidence interval. Colors represent the followup time following diagnosis of HGSOC. In a, *P* values were determined by two-tailed Student's paired t test for matched samples. In C, *P* values were determined by two-tailed Student's t test.

Figure S7. Protein microarray analyses and immunofluorescence staining of intratumoral NK cells in HGSOC. Related to Figure 4 and 6. (A) Protein microarray reactivity analyses of mAb T13, which binds MMP14, and four additional mAbs (T2, T4, T7, T15) that are not reactive

to MMP14. Top 1% hits are presented. Normalized median signal intensities depleted of the background signal (F532 – B532) are plotted against relative fluorescence units (RFU) in Log₁₀ scale. RFU reflects the amount of protein for each target on the array surface. Proteins that contain human IgG Fc domain were disregarded. **(B)** ELISA comparing the reactivity of T13 to MMP14, BSA and ACVR1B – a top membrane-bound hit identified by the protein microarray for T13. Binding to ACVR1B was not detected by ELISA. **(C)** Immunofluorescence staining for CD56, CD3 and DAPI in HGSOc tumors. Representative examples from six patients. In some patients, CD56 expression was detected on tumor cells (patient #31). This phenomenon was previously described, and this type of signal was used as a positive control when no CD56 expressing cells were detected in the tumors. Scale bar, 20µm.

STAR Methods

Resource availability

Lead contact

Further information and requests for resources and reagents should be directed to the lead contact, Ziv Shulman (ziv.shulman@weizmann.ac.il).

Materials availability

Primary cultures and monoclonal antibody expression vectors generated in this study will be distributed upon request.

Data and code availability

- The sequences of monoclonal antibodies that were expressed in this study are available in

Supplementary Table S4. These sequences were deposited in GenBank (OM628888-OM628942, OM628943-OM628997). The raw single-cell immunoglobulin sequencing data is available upon request from the Lead Contact. All clinical parameters for all four cohorts are reported in Supplementary Tables S1-S3, S5 and S7. Due to study participant confidentiality concerns, per patient clinical data cannot be publicly released.

- This paper does not report an original code.
- Any additional information required to reanalyze the data reported in this work paper is available from the Lead Contact upon request.

Experimental model and subject details

Human samples and cohorts

The acquisition of human samples for the purpose of this study was approved by the Helsinki committee of the Rabin Medical Center under protocol 0450-16-RMC and by the Institutional Review Board of the Weizmann Institute of Science under protocol 71-1. Informed consent was obtained from all participants prior to their recruitment to the study. Throughout the study, data were collected based on human samples obtained from four patient cohorts as detailed below. The clinical characteristics of each of these cohorts appear in Supplementary Tables S1-S3 and S5.

Cohort 1 (FFPE samples): A total of 37 FFPE samples were collected from the surgical theatre and department of pathology at the Rabin medical center (29/37) and purchased from the Sheba medical center biobank (8/37). All FFPE specimens in this study were reviewed by a certified gyneco-pathologist to confirm the diagnosis of HGSOE and to ensure sufficient tumor quantity and quality. Moreover, all samples originate from chemo-naïve patients who underwent primary surgery (TAH/BSO) at the time of sample acquisition. 3 samples were removed from the cohort due to poor specimen quality - culminating in 34 FFPE samples; 81.1% of patients in this cohort had stage III-IV disease.

Cohort 2 (ascites samples): A total of 25 ascites samples were obtained from the surgical theatre

and department of gynecologic oncology at the Rabin medical center (7/25) and purchased from the Sheba medical center biobank (18/25). When obtained fresh, fluids were separated to their liquid and cellular phases and cryopreserved accordingly. All cellular samples were preserved in 90% fetal calf serum plus 10% DMSO and stored in liquid nitrogen vapor phase conditions. Fluid samples were flash frozen and stored at -80C. 100% of these patients in this cohort had stage III-IV disease.

Cohort 3 (fresh samples): Fresh tissue samples were obtained from the surgical theatre at the Rabin medical center during the patients' primary surgery (TAH/BSO). Specimens collected included samples of ovarian carcinoma primary tumors, metastases, ascites fluids (enlisted in cohort 2) and peripheral blood as well as samples of healthy ovaries and fallopian tubes from the contralateral non-diseased adnexa, when available. Acquired tissues and tumors were frozen as single cell suspensions and protein extracts, and were also preserved in formalin fixed paraffin embedded (FFPE) tissue blocks (enlisted in cohort 1). Protein extracts were flash frozen and stored at -80C. Samples from a total of 19 chemo-naïve patients were obtained. Of these, 10 patients received a pathological diagnosis of HGSOC and thus were included in this study. The remaining 9 patients were excluded from this cohort based on the following pathological diagnoses: fibrothecoma (2/9), borderline ovarian carcinoma (2/9), granulosa cell tumor (1/9), high grade ovarian leiomyosarcoma (1/9), Low grade endometrial carcinoma with ovarian involvement (1/9), Mucinous ovarian carcinoma (1/9), Primary peritoneal carcinoma (1/9). 100% of patients in this cohort had stage III-IV disease.

Cohort 4 (serum samples from patient in remission): A total of 8 blood samples of HGSOC patients in remission were obtained from the department of gynecological oncology at the Rabin medical center. All patients underwent TAH/BSO, completed their adjuvant therapy and exhibited CA125 values within normal range as well as no evidence of disease on PET/CT. Samples were

collected during routine follow up visits with a mean remission duration of 7.3 months (range: 2.3-17.9 months). At the time of diagnosis, 75% of these patients had stage III-IV disease.

Additional tumor samples: FFPE samples of multiple human tumor types were procured as a tissue microarray (MC5004) from US Biomax.

Study participants

Information about study participants can be found in Supplemental Table S7.

Cell culture conditions

Cell lines and primary cultures were maintained in DMEM media supplemented with 10% (v/v) foetal bovine serum, 1% (v/v) MEM-Eagle non essential amino acids, 1% (v/v) 2mM glutamine and 1% (v/v) Pen-Strep solution. Cells were cultured at 37 °C with 5% carbon dioxide.

Cell lines

ADR/Res, IGROV1, SKOV3, OVCAR3, OVCAR4, OVCAR5, OVCAR8, PANC1, MCF7, HT29, MDAMB435, HEK293T, HEp-2 and K562 were obtained from the Weizmann Institute of Science cell repository. Cell lines originating from the Weizmann Institute of Science cell repository are pre-authenticated and confirmed to be mycoplasma free.

Primary cultures

Fresh HGSOC primary tumor, omental metastases, and ascites samples were retrieved from the operating theatre. Primary cultures were established from these specimens as previously described (O'Donnell et al. 2014) and used after 2-3 passages. Cell preparation included removing fibroblasts as well as all non-adherent cells from the culture. 100% of the cultured cells were EpCAM positive (324207, Biolegend, 1:200). For quantification of tumor IgG binding by flow cytometry, primary cultures were stained for IgG (709-545-149, Jackson ImmunoResearch, 1:200) 24 hours following sample acquisition, and evaluated using a flow cytometer.

Method details

Immunohistochemical and immunofluorescence staining of tissue sections

The following commercial antibodies were used: IgG (709-545-149, Jackson ImmunoResearch, 1:200), CD138 (10593-1-AP, Proteintech, 1:800), CD20 (M0755, Dako, 1:200), CD3 (SP7, Thermo, 1:25), CD56 (AF2408-SP, R&D, 10µg/ml) and MMP14 (LEM-2/15.8, 1:100). Briefly, FFPE specimens were sectioned onto 4µm slides, stained with H&E and evaluated by a certified gynco-pathologist, to assure adequate sample quantity and quality. Unstained slides were then deparaffinized, subjected to antigen retrieval in TE buffer, blocked using 1% bovine serum albumin for 90 minutes, and stained with the appropriate primary and secondary antibodies, overnight at 4°C and for 2 hrs at room temperature, respectively. Slides were then stained with DAPI (1:5000) and sealed using Immunomount.

Quantification of tumor binding by endogenous IgG typed antibodies in FFPE samples

Stained slides were scanned using a 3D Histech Pannoramic SCAN II slide scanner. Post processing of the scanned raw data included identification of all nuclei in the sample using QuPath v0.2.0-m9 cell detection function. Threshold parameters were optimized to identify nuclei of all shapes and sizes, and IgG signal was quantified within a 2µm radius of the nuclear border. An object classifier based on the Random trees (RTrees) machine learning algorithm was trained to distinguish between tumor and non-tumor cell architectures. To negate potential bias, the training was performed on the basis of a multitude of parameters derived from the nuclear data layer (DAPI) only. The software could then distinguish between IgG positive and negative cells and calculate the percentage of IgG-positive cells within each compartment. Quantification of various

populations of immune cells was performed in a similar manner using samples stained for CD138, CD20, IgG, DAPI or CD56 and CD3..

Purification of polyclonal IgG antibody fractions

Polyclonal IgG fractions were isolated from ascites fluids and sera. Briefly, the fluids of interest were filtered through a 0.2µm filter and reacted with protein G Sepharose beads (17-0618-05, Cytiva/GE) on a tilt table, overnight in 4°C. Beads were then pulled down, washed in PBS and eluted using IgG elution buffer (21004, ThermoFisher) into 1M TRIS pH 9. The eluate was then dialyzed against PBS overnight.

Immunofluorescence staining of cell lines and primary cultures

Cell lines or primary cultures of interest were grown on 96 well plates or chamber slides, fixed with 4% PFA, washed with PBS, blocked with 1% BSA for 90 minutes, stained with the antibodies of interest at a concentration of 500nM overnight in 4°C, followed by staining with an Alexa Fluor 488 conjugated secondary antibody and DAPI (1:5000). For fluorescent analysis of monolayers, DAPI normalized Alexa Fluor 488 signal was used to quantify the staining per well using a Synergy HTX plate reader (Biotek). For quantification of immunofluorescence staining, slides were acquired using a Zeiss LSM 880 confocal microscope. The mean fluorescence signal was calculated per cell using QuPath v0.2.0-m9.

ELISA for antibody binding of recombinant proteins

ELISA reactions were carried out using flat-bottom MaxiSorp™ 96-well plates (Invitrogen). Antigen coating was performed in PBS at 100µl per well and left overnight at 4°C. For standard dose response ELISA assays, antigens were plated at a concentration of 1 µg/ml. The enzyme

targets were expressed recombinantly, in house (Udi et al. 2013). For comparative ELISA assays with multiple targets, antigens were plated at a constant molar concentration of 50nM. The plates were washed 5 times with a washing buffer (1× PBS, 0.05% Tween-20) and incubated with 100µl blocking buffer (1× PBS with 1% BSA) for 1h at room temperature. The blocking solution was subsequently replaced by serial dilutions of either mono- or polyclonal antibodies or serum samples for 2.5h at RT. For standard dose response ELISA assays, antibodies were introduced over a range of dilutions whereas for ELISA screens, antibodies were used at 100nM. Serum samples were assayed at a dilution of 1:100. Plates were washed 5 times with a washing buffer and then incubated with anti-human IgG secondary antibody conjugated to horseradish peroxidase (HRP) (Jackson Immuno Research) in PBS at a 1:5,000 dilution. After washing the plates for an additional 5 times, the plates were developed using TMB (Thermo Fisher) and absorbance was measured at 630nm with an ELISA microplate reader (Synergy HTX plate reader, Biotek). ELISA assays for evaluating antibody polyreactivity were performed as previously described (Prigent et al. 2016). For peptide ELISA, the putative epitope sequence of mAb T13 was purchased as a biotinylated peptide from Genscript. Confirmation of peptide binding to mAbs T13 & T12 was performed by coating Maxisorp plates with 5µg/ml of the desired antibody overnight at 4C followed by blocking, incubation with different peptide dilutions, washing (X5), exposure to HRP conjugated streptavidin (1:2000), washing (X5) and TMB development.

Flow cytometric analysis, single ASC sorting and immunoglobulin sequencing

Fresh HGSOc primary tumors retrieved from the operating theatre were immediately dissociated to a single cell suspension in growth medium (DMEM, 10% (v/v) foetal bovine serum, 1% (v/v) MEM-Eagle non essential amino acids, 1% (v/v) 2mM glutamine and 1% (v/v) Pen-Strep

solution.) and placed on ice. Cells were washed in PBS and stained with the following antibodies: Alexa fluor 700 conjugated anti-human CD19 (Biolegend, clone: HIB19), PerCP/Cy5.5 conjugated anti-human CD38 (Biolegend, Clone: HIT2), APC conjugated anti-human IgG1 FC region (RD Systems, Clone: #97924), PE conjugated anti-human IgM (Biolegend, Clone: MHM-88). Samples were stained on ice for 45 minutes, washed and acquired using a Cytoflex flow cytometer and analysed using FlowJo 10.5.3. For immunoglobulin sequencing, tumor infiltrating CD19⁺, CD38⁺⁺, IgM⁻, IgG1⁺, ASCs originating from the primary tumors of 4 HGSOC patients also underwent single cell sorting into 96 well PCR plates containing 4ul per well of mRNA preserving lysis buffer (in RNase free water, 10% DTT 0.1M v/v, 5% PBS X10 v/v, 7.5% RNasin ribonuclease inhibitor v/v, cat: N2615). Sorted plates were immediately frozen to -80C to preserve mRNA integrity. Single cell sorted tumor infiltrating ACSs were reverse transcribed and underwent nested PCR amplification and sequencing of their heavy and light chain transcripts as previously described (Thomas Tiller et al. 2008).

Data analysis of immunoglobulin sequences

Ig Fasta sequences were aligned against the IMGT human heavy chain gene database (downloaded in Dec. 2019) and light chain gene database (downloaded in Feb. 2017) using NCBI IgBlast (version 1.14.0) (Ye et al. 2013). Post processing of IgBlast output and clonal clustering were performed using Change-O v0.4.6 (<https://changeo.readthedocs.io>) (Gupta et al., 2015), Alakazam v0.3.0 (<https://alakazam.readthedocs.io>), SHazaM v0.2.3 (<https://shazam.readthedocs.io>), and custom scripts within the R statistical computing environment, as follows. V(D)J sequences were assigned to clonal groups by partitioning sequences based on identity of IGHV gene annotations, IGHJ gene annotations, and junction region lengths. Within these groups, sequences differing from

one another by more than 15 nucleotides between the V genes were defined as separate clones. Full-length germline sequences were reconstructed for each clone, with the D segment and nucleotide additions in the junction between the V-D and D-J segments) replaced with Ns. Lineage trees were constructed for each clone with at least two unique sequences using the Alakazam R package function, BuildPhylipLineage (Gupta et al. 2015), which utilizes PHYLIP (Felsenstein 2005). In brief, maximum parsimony is a character-based approach that infers a phylogenetic tree by minimizing the total number of steps. The BuildPhylipLineage Alakazam function constructs the immunoglobulin phylogenetic trees through maximum parsimony by an external call to the dnaphars (DNA Parsimony Program) application of the PHYLIP package. The dnaphars program carries out unrooted parsimony on DNA sequences. It assumes that each site evolves independently, that different lineages evolve independently, that the probability of a base substitution at a given site is small over the lengths of time involved in a branch of the phylogeny, and that the expected degree of change in different branches of the phylogeny do not vary by so much that two changes in a high-rate branch are more probable than one change in a low-rate branch. Finally, the expected amounts of change do not vary so much among sites, so that two changes at one site would be more probable than one change at another. Following lineage tree generation, the dnaphars output is changed to allow input sequences to appear as internal nodes of the tree. Intermediate sequences inferred by dnaphars are replaced by progeny within the tree having a Hamming distance of zero from their parent node. The distance calculation allows IUPAC ambiguous character matches, where an ambiguous character has distance zero to any character in the set of characters it represents. Distance calculation and movement of downstream nodes up the tree are repeated until all parent-progeny pairs have a distance greater than zero between them. The germline sequence (outgroup) is moved to the base of the tree and excluded from the node replacement processes, which permits the trunk of the tree to be the only edge with a distance of

zero. Edge weights of the resultant tree are assigned as the distance between each sequence. In selected cases, in which V-J configurations and junction lengths are identical between different sequences for both the heavy and light chains, yet the V genes differed by more than 15 nucleotides, members were manually clustered into single clones, though a common ancestry could not be assumed. Such relations appear with a dashed connecting line in lineage trees. Additionally, multiple identical sequences are treated as a single expanded clone. Selection quantification was calculated using BASELINE's local test (Yaari, Uduman, and Kleinstein 2012).

Antibody expression

ASC immunoglobulin transcripts were chosen for cloning and expression on the basis of several criteria. These included: relation of the candidate to an expanded clone, occurrence of multiple identical clonal members, and high load of somatic hypermutations. Following selection of antibody candidates, constructs containing the heavy and light chain variable regions were produced as gBlocks by IDT and cloned into human IgG1, IgK and IgL expression vectors via the restriction free method. Cloning was performed into human IgG1, IgK and IgL expression vectors (AddGene, AbVec2.0-IGHG1, AbVec1.1-IGKC, AbVec1.1-IGLC2) using Phusion High-Fidelity DNA Polymerase (NEB, cat: M0530L) according to the manufacturer's instructions. The template plasmids were then selectively degraded using the DpnI restriction enzyme (NEB, cat: R0176L) for 16 hours at 37°C. Cloned vectors were transformed into DH5a competent bacteria (Real Biotech) according to the manufacturer's protocol. Plasmid containing bacteria were selected on the basis of vector-acquired ampicillin resistance. After plating, monoclonal bacterial colonies underwent PCR and sequencing validation of their transformed plasmids. Successfully transformed colonies were then expanded and harvested using Qiagen's plasmid purification kit. Purified vectors were transfected into HEK293t cells in 150mm tissue culture plates (Corning) at

12.5ug/DNA per chain using linear 40kDa polyethyleneimine (at a DNA:PEI mass ratio of 1:2) and grown in serum free media for 5 days. Supernatants were filtered through a 0.2µm strainer and reacted with protein G Sepharose beads (17-0618-05, Cytiva/GE) on a tilt table, overnight at 4°C. Beads were then pelleted by centrifugation, washed in PBS and eluted using IgG elution buffer (21004, ThermoFisher) into TRIS pH 9 1M. The eluate was then dialyzed against PBS overnight and its final concentration measured using Nanodrop.

Biolayer interferometry

Analysis of the kinetic binding constants of mAb T13 to MMP14 was performed using the Octet QKe platform. Experiments were conducted at 30°C with shaking at 1,000 rpm. Antibody loading of mAb T13 was performed at an optimized pre-calibrated concentration of 12.5nM for 5 minutes in PBS. Loaded sensors were then exposed to TNC buffer (50mM Tris pH 8, 150mM NaCl, 5mM CaCl₂) for 30 seconds and 1 min in two adjacent wells. Next, MMP14 association was tested over a range of concentrations (30nM-2000nM), in TNC buffer for 30 minutes. Finally, antigen dissociation was followed in TNC buffer for 30 minutes. Data processing, construction of a response model and curve fitting was accomplished using the ForteBio Octet Data analysis software.

Western blot

Cell lysates were made from cell lines and patient derived tumor specimens. Cell lines grown to confluence and minced tumor specimens were emulsified in 500ul of RIPA buffer (20mM Tris pH 7.4, 137mM NaCl, 10% glycerol, 0.1% SDS, 0.5% deoxycholate, 1% triton X-100, 2mM EDTA pH 8, 1mM PMSF, 20uM Leupeptin, in DDW) and protease inhibitor (1:100). Mixture was

vortexed, agitated for 1 hour at 4°C and centrifuged. Supernatants were separated and flash frozen. Prior to the experiment, the protein concentration of the lysates was measured in triplicates using a BCA kit (Pierce™ BCA Protein Assay Kit). Samples containing 25µg of protein were mixed with sample buffer in the presence of DTT, heated to 95°C for 5 minutes and introduced to 15-well gradient gels (Bio-Rad). The gel content was transferred to a nitrocellulose membrane using the rapid transfer method. Nitrocellulose membranes were incubated in blocking buffer (5% BSA, 0.1% tween in PBS) for 1 hour, at room temperature on a tilt table. The membranes were then exposed to the appropriate primary antibodies at 1 µg/ml in 5% BSA in PBS, overnight at 4°C on a tilt table. The next day, membranes were washed 3 times in wash buffer (0.1% tween in PBS), exposed to the appropriate isotype targeting horseradish peroxidase (HRP) conjugated secondary antibodies (Jackson ImmunoResearch) at 1:5000 for 1 hour at room temperature, washed 3 times and developed using ECL. Antibody signals were acquired using the ChemiDoc imaging system (Bio-Rad). Images were analysed using the Image Lab 6.0.1 software (Bio-Rad).

MMP14 overexpression assay

K562 cells were transfected with an *mmp14*:mCherry expression vector using the TransIT-X2 transfection reagent (Mirus Bio) according to the manufacturer's protocol. Briefly, 0.5M K562 cells were plated in 6 well plates in 2.5ml of growth medium (DMEM, 10% (v/v) foetal bovine serum, 1% (v/v) MEM-Eagle non essential amino acids, 1% (v/v) 2mM glutamine and 1% (v/v) Pen-Strep solution) per well. For each condition, in a separate tube, 2.5µg of the *mmp14*:Cherry vector and 7.5µl of the TransIT-X2 transfection reagent were mixed in 250ul of Opti-MEM I reduced serum medium (Gibco) and incubated at room temperature for 30 minutes. Following incubation, the mixture was added to the cells in a drop-wise manner. A mock transfection without the *mmp14*:mCherry construct was performed in parallel as a negative control. Following a 48 hr incubation, the cells were stained with 500nM T13 antibody for 45 minutes on ice, washed, stained

with an Alexa fluor 488 conjugated anti human IgG secondary antibody (Jackson ImmunoResearch) for 30 minutes on ice, washed and analysed using a Cytotflex flow cytometer.

Phage display assay

Biopanning was performed as previously described (Freund, Enshell-Seijffers, and Gershoni 2009). Briefly, approximately 1×10^{10} phages of the random-peptide library were mixed with 2 μg antibody in TBS x1 3% BSA solution (complete to 100 μl) in 0.5 mL vials (AXYGEN, PCR-05-C) and incubated for 1 h on a rotating mixer at RT. Next, 30 μL of protein G coated magnetic beads (Invitrogen, DynabeadsTM Protein G) were added and the mix was incubated for 30 min on a rotating mixer at RT. The vials were then placed on a magnetic stand (Promega, MagneSphere[®] Technology Magnetic Separation Stands) for 2 min and the supernatant was discarded. The magnetically bound beads were washed 3 times with 200 μL wash buffer (TBS x1 0.5% Tween20), re-suspended in 100 μl wash buffer, and transferred to a new vial. The vials were then placed on the magnetic stand and the supernatant was discarded. The bound phages were eluted twice with 105 μL of elution buffer (0.1M HCl adjusted to pH 2.2 with glycine, 1 mg/mL BSA) while rotating at RT for 10 min and neutralized with 19 μL of neutralizing buffer (1M Tris-HCl pH 9.1). Two additional rounds of amplification and biopanning were carried out for each screen. To confirm binding to affinity-selected phages, *E. coli* DH5 α F⁺ were infected with the eluted affinity-selected phages and the bacteria were plated on LB with 20 $\mu\text{g/ml}$ of tetracycline. Single colonies were picked and grown as mini-cultures in U-bottom 96-well cell culture plates (Corning Inc. Life Sciences). The plates were centrifuged to pellet the bacteria and the supernatants were transferred to 96-well flat bottom plates (Greiner Bio-One) containing poly-ethylene glycol/NaCl solution (33% PEG 3.3M NaCl) to precipitate the phages followed by another centrifugation step to pellet the phages. The phages were re-suspended in TBS x1, quantified, and used in dot blot to validate binding by the appropriate antibody. To introduce each sample with its own sample-barcode and

the Illumina adaptors, separate, parallel PCR reactions were conducted. 1 μ L of the eluted phages was mixed with 12.5 μ L high-fidelity DNA polymerase (Invitrogen, PlatinumTM SuperFiTM PCR Master Mix), 10 pmol forward and reverse primers and supplemented with ultra-pure H₂O for a total reaction volume of 25 μ L. The thermal profile was as followed: 98°C for 2 min, 15 cycles of 98°C for 10 sec and 72°C for 5 sec. PCR products were validated by 2% agarose gel, purified by AMPure XP – PCR Purification (Beckman Coulter) and the concentration was measured using Qubit fluorometer. The samples were then diluted to 10 nM, merged, and sent for Illumina NGS sequencing.

Antibody-dependent cellular phagocytosis

Biotinylated MMP14 (2 μ g) protein was used to saturate the binding sites of 0.5mg 1 μ m fluorescent NeutrAvidin beads (Invitrogen). Excess antigen was removed by washing the beads, which were then blocked with 1% BSA. Next, the beads were washed and incubated with antibodies at final concentrations of 0.5 μ M (for monoclonal antibodies) or 1 μ M (for polyclonal antibodies) for 2h at 37°C. Following opsonization, beads were washed, and unbound antibodies were removed. The beads were then either stained for IgG to confirm IgG coating or incubated with phagocytic cells. For the phagocytosis assay, THP-1 cells were added, and the cells were incubated for 1h at 37°C to allow phagocytosis, after which the extent of phagocytosis was measured via flow cytometry (CytoFLEX). For IgG staining, the beads were incubated with anti-human IgG secondary antibody (Jackson Immuno Research) in a blocking buffer at a 1:100 dilution for 30 minutes on ice. The beads were then washed, and the IgG was measured using the CytoFLEX flow cytometer.

Antibody dependent cell-mediated cytotoxicity

Antibody dependent cell-mediated cytotoxicity (ADCC) assays were performed using xCelligence

RTCA DP platform. Briefly, RTCA DP plates were filled with media and measured for background values. Then, OVCAR3 cells were plated at an optimized quantity of 20×10^3 cells per well on RTCA DP plates. OVCAR3 cell proliferation during the seeding phase was monitored via their cell index value. 24 hours after seeding, the cells were incubated with monoclonal or polyclonal antibodies at 500nM for 1 hour in PBS, and mixed with lymphokine activated donor natural killer cells at various effector to target (E:T) ratios. Upon introduction of the effector cells, the viability of the OVCAR3 tumor cell population was monitored over a 24-72 hour period. Prior to the ADCC assay, NK cells were isolated from the peripheral blood of healthy donors using the EasySep human NK cell enrichment kit (STEMCELL), and activated by incubation in growth media in the presence of 500IU/ml human recombinant IL-2 overnight.

Analysis of previously published RNA expression data

RNA-seq counts were obtained from Gene Expression Omnibus (GSE102094, GSE71340). Differential expression analysis between HGSOC patients and normal tissues was performed by using DESeq2 (Love et al, Genome Biology, 2014 / 25516281).

Retrospective estimation of the risk for autoimmunity among ovarian cancer patients

Estimation of the risk for autoimmunity was performed based on data from the electronic health record (EHR) database from Clalit Healthcare Services (Balicer and Afek 2017). In this analysis we evaluated women aged 40-80 years between 2005-2020. Two cohorts were defined: an autoimmune cohort and an ovarian cancer cohort. Female patients were included in the autoimmune cohort pending a previously documented ICD-9 code corresponding to the diagnosis of an autoimmune disease in their medical records. These included: systemic lupus erythematosus (710.0), rheumatoid arthritis (L88 / 714.5 / 714.2 / 714 / 714.0), systemic sclerosis and other forms

of scleroderma (710.1 / 701.0), ankylosing spondylitis (720.0), dermatomyositis (710.3), polymyositis (710.4), Sjögren syndrome (710.2), psoriatic arthropathy (696.0), polyarteritis nodosa (446.0), chronic postrheumatic arthropathy (714.4), polymyalgia rheumatica (725), inflammatory polyarthropathy (714.9) and other rheumatic and connective tissue diseases (729 / 710 / 710.9 / 710.8 / 710.5). The onset of diagnosis was adjusted upon evidence of prior therapy for autoimmune diseases (methotrexate / hydroxychloroquine) or a diagnosis of palindromic rheumatism (719.3) in the three years preceding the diagnosis of autoimmunity. Female patients were included in the ovarian cancer cohort pending a previously documented ICD-9 code indicating a diagnosis of ovarian cancer in the patient's medical records (ICD-9 codes: 183.9, 183.8, 183.2, 183.0, 183). The onset of ovarian cancer diagnosis was adjusted upon evidence of prior administration of chemotherapy (carboplatin / paclitaxel / topotecan) or traditional antiemetics (ondansetron, granisetron) in the five years preceding the diagnosis. Onset was also adjusted in case of the following ICD 9 diagnoses: malignant neoplasm of uterus, part unspecified (179), unspecified malignant neoplasm (D77/ W72) and excision or destruction of peritoneal tissue (Z54.4) in the five years preceding the diagnosis - or - abdominal or pelvic swelling, mass or lump (789.3), ascites (789.5) or unspecified ovarian cyst (620.2) in the two years preceding the diagnosis. Patients with previous diagnoses of other malignancies were excluded as well as patients who had a diagnosis of an autoimmune disease preceding their ovarian cancer diagnosis. Controls were sampled from the general population and consisted of females who were not diagnosed with ovarian cancer and who were matched to the ovarian cancer cohort patients based on age and calendar year. In the ovarian cancer cohort and controls, the number of patients diagnosed with an autoimmune disease was counted during the followup period. The binomial estimate for the probability to have an autoimmune disease in a single month was calculated by dividing the number of patients who were diagnosed with an autoimmune disease in a given cohort,

by the cumulative number of patient-months available in a given follow up period. The ovarian cancer cohort included 3,353 patients contributing up to 179,555 patient months to the analysis, while the control included 43,589 matched controls contributing up to 2,549,627 patient months. Thus, an annual incidence rate was calculated per 100,000 patients as well as a confidence interval, for followup periods of 1, 5, 10 and 15 years.

Antigen microarray

Human Protein Microarray (ProtoArray) was used to measure antibody binding against a panel of proteins absorbed on the surface (Cat #PAH05251020, Invitrogen). Microarrays were blocked for 1 hour at RT with 2% bovine serum albumin and incubated under a coverslip overnight at 4°C with 10 µg patient purified antibodies in blocking buffer (2% BSA in TBS). The arrays were then washed (X3 with 0.05% Tween20) and incubated for 2 hour at RT with a goat anti-human IgG Cy3-conjugated antibody ((1:250), Jackson ImmunoResearch Laboratories Inc, CAT#109-165-003.). The arrays were then washed (X3 with 0.05% Tween20), dried and scanned using InnoScan 710 (INNOPSYS) at 532 nm.

Antigen microarray data processing and background filtering

For each spot, the intensity was defined as the mean fluorescence intensity minus the localized background intensity (denoted F532-B532). Then, the average of two technical replicates in each chip was normalized by its median reactivity to account for differences in total protein concentrations that affect the background intensity level. The amount of material deposited in each spot was provided by the manufacturer based on the measurement of the GST tag of the absorbed protein. Signal intensity for each spot was then normalized to the GST signal. Proteins that contained a region from human Fc region (as indicated by the manufacturer) which can be bound by secondary anti-human Fc were not included in the analysis.

Patient survival analysis

The clinical data was collected from the medical records of 34 recruited HGSOc patients for whom FFPE specimens of their primary tumor were available. In order to minimize potential biases, the cohort of patients was designed to be as homogenous as possible in terms of disease progression and survival-influencing factors – such as disease stage at presentation, debulking status and adjuvant treatment. All the patients recruited underwent primary debulking surgery (total abdominal hysterectomy with bilateral salpingo-oophorectomy) without receiving prior neoadjuvant chemotherapy. Following surgery, all patients received taxane and platinum-based standard of care adjuvant chemotherapy. All patients were regularly followed up by their gynecologists. Of note, none of the patients recruited experienced intraoperative or perioperative complications or perished from aetiologies unrelated to their malignancy. Overall survival (OS) was calculated as the time interval between diagnosis and death, or last follow-up if the patient did not succumb to her disease. Progression free survival (PFS) was calculated as the time between primary surgery and the date in which the first objective evidence of recurrence was recorded, or last follow up if the patient did not experience disease recurrence. One patient was omitted from the PFS analysis due to inconclusive data relating to her date of disease recurrence. OS and PFS were correlated to data retrieved from immunofluorescence staining of the primary tumors, namely, the percentage of IgG coated tumor cells and the abundance of IgG⁺ ASCs in the tumor microenvironment. Tumors which exhibited positive IgG staining in less than 10% of their cells were considered IgG⁻, whereas staining equal to or greater than 10% was considered IgG⁺. For infiltration of IgG⁺ ASCs, an average number of 100 IgG⁺ ASCs per high power field (HPF) was established as the threshold value. This was determined following computational quantification of IgG⁺ ASCs in three independent HPFs per patient. These data were used to construct Kaplan-Meier curves. Statistical significance between the curves was determined using the log-rank (Mantel-

Cox) test.

Structure prediction and docking analysis

The amino acid sequence of T13 antibody VDJ region

(VH:EVQLVESGGGLVQPGGSLRLSCAASGIFISKHDMYWVRQRPKGLEWVSRIGDAG
DTYYAGSVKGRFTIFRENAKNTLYFQMNRLTDGDTAVYYCGRGMAVAGFPLDVWGR
GTRVTVTS;

VL:EIVMTQSPATLSVSPGERATLSCRASQNIHINLAWYQQKPGQAPRLIYAASTRAAGI
PARFSASGSGTEFTLTISSLQSEDFAVYYCQQFNPWSPWTFGQGTKVEVK) was computed on the "advanced" Google Colab cloud interface using the AlphaFold framework (Jumper et al. 2021). Multiple sequence alignments (MSAs) were generated using MMseqs2 and analysis resulted in five models that were sorted by their pLDDT score. The top-ranked model was then docked to MMP14 (PDB 5H0U) via Global Docking analysis using the PatchDock algorithm (Schneidman-Duhovny et al. 2005) followed by protein-protein refinement stage on the FireDock server (Mashiach et al. 2008). Final complexes were assessed for their binding site and cross-referenced with the phage display hits.

Statistical analysis

The D'Agostino-Pearson and Shapiro-Wilk normality tests were employed to assess the normality of our data. Normally and near-normally distributed datasets were evaluated using parametric statistical tests such as one way ANOVA and student's paired / unpaired t-test, as appropriate. Normality was assumed in datasets which were too small to be tested for normality. Non-normally distributed datasets were mainly of lognormal distribution. These datasets were tested using non-

parametric tests such as the Kruskal-Wallis test and the Mann–Whitney U test. Post-hoc analyses were performed following each relevant test. For one way ANOVA, we used Dunnett’s post-hoc test and for Kruskal-Wallis test, we used Dunn’s post-hoc test. For survival analyses, we used the log-rank (Mantel-Cox) test to determine the difference between Kaplan Meier plots. Correlation between datasets composed of continuous variables was performed using Pearson’s correlation coefficient and fitting of a linear regression model. Differential gene expression analysis was performed using DESeq2.

Supplementary spread sheet table titles

Supplementary Table S4. Sequences, genes, clones and reactivities of monoclonal antibodies. Related to Figure 3.

Supplementary Table S6. Protein microarray data. Related to Figure 4.

Supplementary Table S7. Study participants. Related to STAR methods.

References

- Anderson, Karen S., Daniel W. Cramer, Sahar Sibani, Garrick Wallstrom, Jessica Wong, Jin Park, Ji Qiu, Allison Vitonis, and Joshua LaBaer. 2015. "Autoantibody Signature for the Serologic Detection of Ovarian Cancer." *Journal of Proteome Research*. <https://doi.org/10.1021/pr500908n>.
- Andreu, Pauline, Magnus Johansson, Nesrine I. Affara, Ferdinando Pucci, Tingting Tan, Simon Junankar, Lidiya Korets, et al. 2010. "FcR γ Activation Regulates Inflammation-Associated Squamous Carcinogenesis." *Cancer Cell* 17 (2): 121–34.
- Andrusier, Nelly, Ruth Nussinov, and Haim J. Wolfson. 2007. "FireDock: Fast Interaction Refinement in Molecular Docking." *Proteins* 69 (1): 139–59.
- Ashkenazy, Haim, Oren Avram, Arie Ryvkin, Anna Roitburd-Berman, Yael Weiss-Ottolenghi, Smadar Hada-Neeman, Jonathan M. Gershoni, and Tal Pupko. 2021. "Motifier: An IgOme Profiler Based on Peptide Motifs Using Machine Learning." *Journal of Molecular Biology*. <https://doi.org/10.1016/j.jmb.2021.167071>.
- Auersperg, Nelly. 2013. "Ovarian Surface Epithelium as a Source of Ovarian Cancers: Unwarranted Speculation or Evidence-Based Hypothesis?" *Gynecologic Oncology* 130 (1): 246–51.
- Balicer, Ran D., and Arnon Afek. 2017. "Digital Health Nation: Israel's Global Big Data Innovation Hub." *The Lancet*.
- Bankhead, Peter, Maurice B. Loughrey, José A. Fernández, Yvonne Dombrowski, Darragh G. McArt, Philip D. Dunne, Stephen McQuaid, et al. 2017. "QuPath: Open Source Software for Digital Pathology Image Analysis." *Scientific Reports* 7 (1): 16878.
- Biram, Adi, Natalia Davidzohn, and Ziv Shulman. 2019. "T Cell Interactions with B Cells during Germinal Center Formation, a Three- step Model." *Immunological Reviews* 288 (1): 37–48.
- Biswas, Subir, Gunjan Mandal, Kyle K. Payne, Carmen M. Anadon, Chandler D. Gatenbee, Ricardo A. Chaurio, Tara Lee Costich, et al. 2021. "IgA Transcytosis and Antigen Recognition Govern Ovarian Cancer Immunity." *Nature* 591 (7850): 464–70.
- Boland, Julia L., Qin Zhou, Madhuri Martin, Margaret K. Callahan, Jason Konner, Roisin E. O'Cearbhaill, Claire F. Friedman, et al. 2019. "Early Disease Progression and Treatment Discontinuation in Patients with Advanced Ovarian Cancer Receiving Immune Checkpoint Blockade." *Gynecologic Oncology* 152 (2): 251–58.
- Bolotin, Dmitriy A., Stanislav Poslavsky, Alexey N. Davydov, Felix E. Frenkel, Lorenzo Fanchi, Olga I. Zolotareva, Saskia Hemmers, et al. 2017. "Antigen Receptor Repertoire Profiling from RNA-Seq Data." *Nature Biotechnology* 35 (10): 908–11.
- Bowtell, David D. L. 2010. "The Genesis and Evolution of High-Grade Serous Ovarian Cancer." *Nature Reviews. Cancer* 10 (11): 803–8.
- Cabrita, Rita, Martin Lauss, Adriana Sanna, Marco Donia, Mathilde Skaarup Larsen, Shamik Mitra, Iva Johansson, et al. 2020. "Tertiary Lymphoid Structures Improve Immunotherapy and Survival in Melanoma." *Nature* 577 (7791): 561–65.
- Cathcart, Jillian M., Anna Banach, Alice Liu, Jun Chen, Michael Goligorsky, and Jian Cao. 2016. "Interleukin-6 Increases Matrix Metalloproteinase-14 (MMP-14) Levels via down-Regulation of p53 to Drive Cancer Progression." *Oncotarget* 7 (38): 61107–20.
- Cho, Angela, Viive M. Howell, and Emily K. Colvin. 2015. "The Extracellular Matrix in Epithelial Ovarian Cancer - A Piece of a Puzzle." *Frontiers in Oncology* 5 (November): 245.
- Cornaby, Caleb, Lauren Gibbons, Vera Mayhew, Chad S. Sloan, Andrew Welling, and Brian D.

- Poole. 2015. "B Cell Epitope Spreading: Mechanisms and Contribution to Autoimmune Diseases." *Immunology Letters* 163 (1): 56–68.
- Crowley, Jameson T., Klemen Strle, Elise E. Drouin, Annalisa Pianta, Sheila L. Arvikar, Qi Wang, Catherine E. Costello, and Allen C. Steere. 2016. "Matrix Metalloproteinase-10 Is a Target of T and B Cell Responses That Correlate with Synovial Pathology in Patients with Antibiotic-Refractory Lyme Arthritis." *Journal of Autoimmunity* 69 (May): 24–37.
- Cui, Can, Jiawei Wang, Ping-Min Chen, Kelli Connolly, Martina Damo, Eric Fagerberg, Shuting Chen, et al. n.d. "Neoantigen Driven B Cell and CD4 T Follicular Helper Cell Collaboration Promotes Robust Anti-Tumor CD8 T Cell Responses." *SSRN Electronic Journal*. <https://doi.org/10.2139/ssrn.3751671>.
- Degn, Søren E., Cees E. van der Poel, Daniel J. Firl, Burcu Ayoglu, Fahd A. Al Qureshah, Goran Bajic, Luka Mesin, et al. 2017. "Clonal Evolution of Autoreactive Germinal Centers." *Cell* 170 (5): 913–26.e19.
- DeNardo, David G., and Brian Ruffell. 2019. "Macrophages as Regulators of Tumour Immunity and Immunotherapy." *Nature Reviews. Immunology* 19 (6): 369–82.
- DeWeerd, Sarah. 2021. "The Origins of Ovarian Cancer." *Nature* 600 (7889): S42–44.
- DiLillo, D. J., and J. V. Ravetch. 2015. "Fc-Receptor Interactions Regulate Both Cytotoxic and Immunomodulatory Therapeutic Antibody Effector Functions." *Cancer Immunology Research*. <https://doi.org/10.1158/2326-6066.cir-15-0120>.
- Di Zenzo, Giovanni, Giulia Di Lullo, Davide Corti, Valentina Calabresi, Anna Sinistro, Fabrizia Vanzetta, Biagio Didona, et al. 2012. "Pemphigus Autoantibodies Generated through Somatic Mutations Target the Desmoglein-3 Cis-Interface." *The Journal of Clinical Investigation* 122 (10): 3781–90.
- Doo, David W., Lyse A. Norian, and Rebecca C. Arend. 2019. "Checkpoint Inhibitors in Ovarian Cancer: A Review of Preclinical Data." *Gynecologic Oncology Reports* 29 (August): 48–54.
- Duhovny, D., R. Nussinov, and H. Wolfson. n.d. "Efficient Unbound Docking of Rigid Molecules In Gusfield et Al., Ed." In *Proceedings of the 2'nd Workshop on Algorithms in Bioinformatics (WABI) Rome, Italy, Lecture Notes in Computer Science*. Vol. 2452.
- Felsenstein, J. 2005. "PHYLIP (phylogeny Inference Package) Version 3.6. Distributed by the Author. Seattle (WA): Department of Genome Sciences, University of Washington."
- Freund, Natalia Tarnovitski, David Enshell-Seijffers, and Jonathan M. Gershoni. 2009. "Phage Display Selection, Analysis, and Prediction of B Cell Epitopes." *Current Protocols in Immunology / Edited by John E. Coligan ... [et Al.]* Chapter 9 (August): Unit 9.8.
- Gnjatic, Sacha, Erika Ritter, Markus W. Büchler, Nathalia A. Giese, Benedikt Brors, Claudia Frei, Anne Murray, et al. 2010. "Seromic Profiling of Ovarian and Pancreatic Cancer." *Proceedings of the National Academy of Sciences of the United States of America* 107 (11): 5088–93.
- Gupta, Namita T., Jason A. Vander Heiden, Mohamed Uduman, Daniel Gadala-Maria, Gur Yaari, and Steven H. Kleinstein. 2015. "Change-O: A Toolkit for Analyzing Large-Scale B Cell Immunoglobulin Repertoire Sequencing Data." *Bioinformatics* 31 (20): 3356–58.
- Helmink, Beth A., Sangeetha M. Reddy, Jianjun Gao, Shaojun Zhang, Rafet Basar, Rohit Thakur, Keren Yizhak, et al. 2020. "B Cells and Tertiary Lymphoid Structures Promote Immunotherapy Response." *Nature* 577 (7791): 549–55.
- Hu, Xihao, Jian Zhang, Jin Wang, Jingxin Fu, Taiwen Li, Xiaoqi Zheng, Binbin Wang, et al. 2019. "Landscape of B Cell Immunity and Related Immune Evasion in Human Cancers." *Nature Genetics* 51 (3): 560–67.
- Jayson, Gordon C., Elise C. Kohn, Henry C. Kitchener, and Jonathan A. Ledermann. 2014. "Ovarian Cancer." *The Lancet* 384 (9951): 1376–88.

- Jumper, John, Richard Evans, Alexander Pritzel, Tim Green, Michael Figurnov, Olaf Ronneberger, Kathryn Tunyasuvunakool, et al. 2021. "Highly Accurate Protein Structure Prediction with AlphaFold." *Nature* 596 (7873): 583–89.
- Kaimal, Rajani, Raid Aljumaily, Sarah L. Tressel, Rutika V. Pradhan, Lidija Covic, Athan Kuliopulos, Corrine Zarwan, Young B. Kim, Sheida Sharifi, and Anika Agarwal. 2013. "Selective Blockade of Matrix Metalloprotease-14 with a Monoclonal Antibody Abrogates Invasion, Angiogenesis, and Tumor Growth in Ovarian Cancer." *Cancer Research* 73 (8): 2457–67.
- Kamel, Hossam, Ibrahim Abdelazim, Sherif M. Habib, Mahmoud A. A. El Shourbagy, and Naglaa Samier Ahmed. 2010. "Immunoexpression of Matrix Metalloproteinase-2 (MMP-2) in Malignant Ovarian Epithelial Tumours." *Journal of Obstetrics and Gynaecology Canada*. [https://doi.org/10.1016/s1701-2163\(16\)34527-3](https://doi.org/10.1016/s1701-2163(16)34527-3).
- Kroeger, David R., Katy Milne, and Brad H. Nelson. 2016. "Tumor-Infiltrating Plasma Cells Are Associated with Tertiary Lymphoid Structures, Cytolytic T-Cell Responses, and Superior Prognosis in Ovarian Cancer." *Clinical Cancer Research: An Official Journal of the American Association for Cancer Research* 22 (12): 3005–15.
- Labidi-Galy, S. Intidhar, Eniko Papp, Dorothy Hallberg, Noushin Niknafs, Vilmos Adleff, Michael Noe, Rohit Bhattacharya, et al. 2017. "High Grade Serous Ovarian Carcinomas Originate in the Fallopian Tube." *Nature Communications* 8 (1): 1093.
- Mahmood, Reem D., Robert D. Morgan, Richard J. Edmondson, Andrew R. Clamp, and Gordon C. Jayson. 2020. "First-Line Management of Advanced High-Grade Serous Ovarian Cancer." *Current Oncology Reports* 22 (6): 64.
- Maletzki, Claudia, Annika Jahnke, Christiane Ostwald, Ernst Klar, Friedrich Prall, and Michael Linnebacher. 2012. "Ex-Vivo Clonally Expanded B Lymphocytes Infiltrating Colorectal Carcinoma Are of Mature Immunophenotype and Produce Functional IgG." *PloS One* 7 (2): e32639.
- Mashiach, Efrat, Dina Schneidman-Duhovny, Nelly Andrusier, Ruth Nussinov, and Haim J. Wolfson. 2008. "FireDock: A Web Server for Fast Interaction Refinement in Molecular Docking." *Nucleic Acids Research* 36 (Web Server issue): W229–32.
- Ma, Yan, Xiao Wang, Cuipeng Qiu, Jiejie Qin, Keyan Wang, Guiying Sun, Di Jiang, et al. 2020. "Using Protein Microarray to Identify and Evaluate Autoantibodies to Tumor-Associated Antigens in Ovarian Cancer." *Cancer Science*, November. <https://doi.org/10.1111/cas.14732>.
- Mietzner, Brun, Makoto Tsuiji, Johannes Scheid, Klara Velinzon, Thomas Tiller, Klaus Abraham, Jose B. Gonzalez, et al. 2008. "Autoreactive IgG Memory Antibodies in Patients with Systemic Lupus Erythematosus Arise from Nonreactive and Polyreactive Precursors." *Proceedings of the National Academy of Sciences of the United States of America* 105 (28): 9727–32.
- Milne, Katy, Rebecca O. Barnes, Adam Girardin, Melanie A. Mawer, Nancy J. Nesslinger, Alvin Ng, Julie S. Nielsen, et al. 2008. "Tumor-Infiltrating T Cells Correlate with NY-ESO-1-Specific Autoantibodies in Ovarian Cancer." *PloS One* 3 (10): e3409.
- Mirdita, Milot, Konstantin Schütze, Yoshitaka Moriwaki, Lim Heo, Sergey Ovchinnikov, and Martin Steinegger. 2021. "ColabFold - Making Protein Folding Accessible to All." *Research Square*. <https://doi.org/10.21203/rs.3.rs-1032816/v1>.
- Montfort, Anne, Oliver Pearce, Eleni Maniati, Benjamin G. Vincent, Lisa Bixby, Steffen Böhm, Thomas Dowe, et al. 2017. "A Strong B-Cell Response Is Part of the Immune Landscape in Human High-Grade Serous Ovarian Metastases." *Clinical Cancer Research: An Official Journal of the American Association for Cancer Research* 23 (1): 250–62.

- Mose, Lisle E., Sara R. Selitsky, Lisa M. Bixby, David L. Marron, Michael D. Iglesia, Jonathan S. Serody, Charles M. Perou, Benjamin G. Vincent, and Joel S. Parker. 2016. "Assembly-Based Inference of B-Cell Receptor Repertoires from Short Read RNA Sequencing Data with V'DJer." *Bioinformatics* 32 (24): 3729–34.
- Moss, Natalie M., Maria V. Barbolina, Yueying Liu, Limin Sun, Hidayatullah G. Munshi, and M. Sharon Stack. 2009. "Ovarian Cancer Cell Detachment and Multicellular Aggregate Formation Are Regulated by Membrane Type 1 Matrix Metalloproteinase: A Potential Role in I.p. Metastatic Dissemination." *Cancer Research* 69 (17): 7121–29.
- Nelson, Brad H. 2010. "CD20+ B Cells: The Other Tumor-Infiltrating Lymphocytes." *Journal of Immunology* 185 (9): 4977–82.
- Nishijima, C., I. Hayakawa, T. Matsushita, K. Komura, M. Hasegawa, K. Takehara, and S. Sato. 2004. "Autoantibody against Matrix Metalloproteinase-3 in Patients with Systemic Sclerosis." *Clinical and Experimental Immunology*. <https://doi.org/10.1111/j.1365-2249.2004.02615.x>.
- Nzula, Sazini, James J. Goings, and David I. Stott. 2003. "Antigen-Driven Clonal Proliferation, Somatic Hypermutation, and Selection of B Lymphocytes Infiltrating Human Ductal Breast Carcinomas." *Cancer Research* 63 (12): 3275–80.
- O'Donnell, Rachel L., Aiste McCormick, Asima Mukhopadhyay, Laura C. Woodhouse, Madeleine Moat, Anna Grundy, Michelle Dixon, et al. 2014. "The Use of Ovarian Cancer Cells from Patients Undergoing Surgery to Generate Primary Cultures Capable of Undergoing Functional Analysis." *PloS One* 9 (6): e90604.
- Petitprez, Florent, Aurélien de Reyniès, Emily Z. Keung, Tom Wei-Wu Chen, Cheng-Ming Sun, Julien Calderaro, Yung-Ming Jeng, et al. 2020. "B Cells Are Associated with Survival and Immunotherapy Response in Sarcoma." *Nature* 577 (7791): 556–60.
- Piccoli, Luca, Ilaria Campo, Chiara Silacci Fregni, Blanca Maria Fernandez Rodriguez, Andrea Minola, Federica Sallusto, Maurizio Luisetti, Davide Corti, and Antonio Lanzavecchia. 2015. "Neutralization and Clearance of GM-CSF by Autoantibodies in Pulmonary Alveolar Proteinosis." *Nature Communications* 6 (June): 7375.
- Pitzalis, Costantino, Gareth W. Jones, Michele Bombardieri, and Simon A. Jones. 2014. "Ectopic Lymphoid-like Structures in Infection, Cancer and Autoimmunity." *Nature Reviews Immunology* 14 (7): 447–62.
- Prigent, Julie, Valérie Lorin, Ayrin Kök, Thierry Hieu, Salomé Bourgeau, and Hugo Mouquet. 2016. "Scarcity of Autoreactive Human Blood IgA+ Memory B Cells." *European Journal of Immunology* 46 (10): 2340–51.
- Ramalingam, Preetha. 2016. "Morphologic, Immunophenotypic, and Molecular Features of Epithelial Ovarian Cancer." *Oncology* 30 (2): 166–76.
- Ran, M., G. Klein, and I. P. Witz. 1976. "Tumor-Bound Immunoglobulins. Evidence for the in Vivo Coating of Tumor Cells by Potentially Cytotoxic Anti-Tumour Antibodies." *International Journal of Cancer. Journal International Du Cancer* 17 (1): 90–97.
- Rao, G. Subba, G. Subba Rao, and Parviz Hanjani. 1988. "Detection of Human Ovarian Tumor-Associated Antigens by Antibodies Isolated from Ovarian Carcinoma Ascitic Fluid." *American Journal of Obstetrics and Gynecology*. [https://doi.org/10.1016/0002-9378\(88\)90500-5](https://doi.org/10.1016/0002-9378(88)90500-5).
- Sakata, K., K. Shigemasa, N. Nagai, and K. Ohama. 2000. "Expression of Matrix Metalloproteinases (MMP-2, MMP-9, MT1-MMP) and Their Inhibitors (TIMP-1, TIMP-2) in Common Epithelial Tumors of the Ovary." *International Journal of Oncology*. <https://doi.org/10.3892/ijo.17.4.673>.
- Sato, Shinichi, Ikuko Hayakawa, Minoru Hasegawa, Kazuhiko Takehara, and Manabu Fujimoto.

2003. "Function Blocking Autoantibodies Against Matrix Metalloproteinase-1 in Patients with Systemic Sclerosis." *Journal of Investigative Dermatology*.
<https://doi.org/10.1046/j.1523-1747.2003.12097.x>.
- Saul, Louise, Kristina M. Ilieva, Heather J. Bax, Panagiotis Karagiannis, Isabel Correa, Irene Rodriguez-Hernandez, Debra H. Josephs, et al. 2016. "IgG Subclass Switching and Clonal Expansion in Cutaneous Melanoma and Normal Skin." *Scientific Reports* 6 (July): 29736.
- Schneidman-Duhovny, Dina, Yuval Inbar, Ruth Nussinov, and Haim J. Wolfson. 2005. "PatchDock and SymmDock: Servers for Rigid and Symmetric Docking." *Nucleic Acids Research* 33 (Web Server issue): W363–67.
- Schroeder, Kristin, Martin Herrmann, and Thomas H. Winkler. 2013. "The Role of Somatic Hypermutation in the Generation of Pathogenic Antibodies in SLE." *Autoimmunity* 46 (2): 121–27.
- Sharonov, George V., Ekaterina O. Serebrovskaya, Diana V. Yuzhakova, Olga V. Britanova, and Dmitriy M. Chudakov. 2020. "B Cells, Plasma Cells and Antibody Repertoires in the Tumour Microenvironment." *Nature Reviews. Immunology* 20 (5): 294–307.
- Silburn, P. A., S. K. Khoo, R. Hill, B. Daunter, and E. V. Mackay. 1984. "Demonstration of Tumor-Associated Immunoglobulin G Isolated from Immune Complexes in Ascitic Fluid of Ovarian Cancer." *Diagnostic Immunology* 2 (1): 30–35.
- Tiller, Thomas, Eric Meffre, Sergey Yurasov, Makoto Tsuiji, Michel C. Nussenzweig, and Hedda Wardemann. 2008. "Efficient Generation of Monoclonal Antibodies from Single Human B Cells by Single Cell RT-PCR and Expression Vector Cloning." *Journal of Immunological Methods* 329 (1-2): 112–24.
- Tiller, Thomas, Makoto Tsuiji, Sergey Yurasov, Klara Velinzon, Michel C. Nussenzweig, and Hedda Wardemann. 2007. "Autoreactivity in Human IgG+ Memory B Cells." *Immunity* 26 (2): 205–13.
- Tiller, T., E. Meffre, S. Yurasov, M. Tsuiji, and M. C. Nussenzweig. n.d. "H. 494 Wardemann. 2008. Efficient Generation of Monoclonal Antibodies from Single 495 Human B Cells by Single Cell RT-PCR and Expression Vector Cloning." *Journal of* 496: 112–24.
- Udi, Y., M. Fragai, M. Grossman, S. Mitternacht, R. Arad-Yellin, V. Calderone, M. Melikian, et al. 2013. "Unraveling Hidden Allosteric Regulatory Sites in Structurally Homologues Metalloproteases." Worldwide Protein Data Bank. <https://doi.org/10.2210/pdb4ijo/pdb>.
- Uppendahl, Locke D., Carly M. Dahl, Jeffrey S. Miller, Martin Felices, and Melissa A. Geller. 2017. "Natural Killer Cell-Based Immunotherapy in Gynecologic Malignancy: A Review." *Frontiers in Immunology* 8: 1825.
- Victora, Gabriel D., and Michel C. Nussenzweig. 2012. "Germinal Centers." *Annual Review of Immunology* 30 (January): 429–57.
- Vinuesa, Carola G., Iñaki Sanz, and Matthew C. Cook. 2009. "Dysregulation of Germinal Centres in Autoimmune Disease." *Nature Reviews. Immunology* 9 (12): 845–57.
- Vos, Maria Caroline, Eva Hollemans, Nicole Ezendam, Harry Feijen, Dorry Boll, Brenda Pijlman, Hans van der Putten, et al. 2016. "MMP-14 and CD44 in Epithelial-to-Mesenchymal Transition (EMT) in Ovarian Cancer." *Journal of Ovarian Research* 9 (1): 53.
- Vos, M. Caroline, Anneke A. M. van der Wurff, Toin H. van Kuppevelt, and Leon F. A. G. Massuger. 2021. "The Role of MMP-14 in Ovarian Cancer: A Systematic Review." *Journal of Ovarian Research* 14 (1): 1–13.
- Wang, Eric Y., Tianyang Mao, Jon Klein, Yile Dai, John D. Huck, Feimei Liu, Neil S. Zheng, et al. 2020. "Diverse Functional Autoantibodies in Patients with COVID-19." *medRxiv : The Preprint Server for Health Sciences*, December.

- <https://doi.org/10.1101/2020.12.10.20247205>.
- Wardemann, Hedda, Sergey Yurasov, Anne Schaefer, James W. Young, Eric Meffre, and Michel C. Nussenzweig. 2003. "Predominant Autoantibody Production by Early Human B Cell Precursors." *Science* 301 (5638): 1374–77.
- Webb, Nicholas E., Biana Bernshtein, and Galit Alter. 2021. "Tissues: The Unexplored Frontier of Antibody Mediated Immunity." *Current Opinion in Virology* 47 (April): 52–67.
- Wieland, Andreas, and Rafi Ahmed. 2019. "Fc Receptors in Antimicrobial Protection." *Current Topics in Microbiology and Immunology* 423: 119–50.
- Wieland, Andreas, Mihir R. Patel, Maria A. Cardenas, Christiane S. Eberhardt, William H. Hudson, Rebecca C. Obeng, Christopher C. Griffith, et al. 2020. "Defining HPV-Specific B Cell Responses in Patients with Head and Neck Cancer." *Nature*, November.
<https://doi.org/10.1038/s41586-020-2931-3>.
- Witz, Isaac P. 1977. "Tumor-Bound Immunoglobulins: In Situ Expressions Of Humoral Immunity." *Advances in Cancer Research* 25: 95–148.
- Yaari, Gur, Mohamed Uduman, and Steven H. Kleinstein. 2012. "Quantifying Selection in High-Throughput Immunoglobulin Sequencing Data Sets." *Nucleic Acids Research* 40 (17): e134.
- Yang, Fan, Sandra C. A. Nielsen, Ramona A. Hoh, Katharina Röltgen, Oliver Fabian Wirz, Emily Haraguchi, Grace H. Jean, et al. 2021. "Shared B Cell Memory to Coronaviruses and Other Pathogens Varies in Human Age Groups and Tissues." *Science*, April.
<https://doi.org/10.1126/science.abf6648>.
- Ye, Jian, Ning Ma, Thomas L. Madden, and James M. Ostell. 2013. "IgBLAST: An Immunoglobulin Variable Domain Sequence Analysis Tool." *Nucleic Acids Research* 41 (Web Server issue): W34–40.
- Zaenker, P., E. S. Gray, and M. R. Ziman. 2016. "Autoantibody Production in Cancer—The Humoral Immune Response toward Autologous Antigens in Cancer Patients." *Autoimmunity Reviews* 15 (5): 477–83.

Fig 1

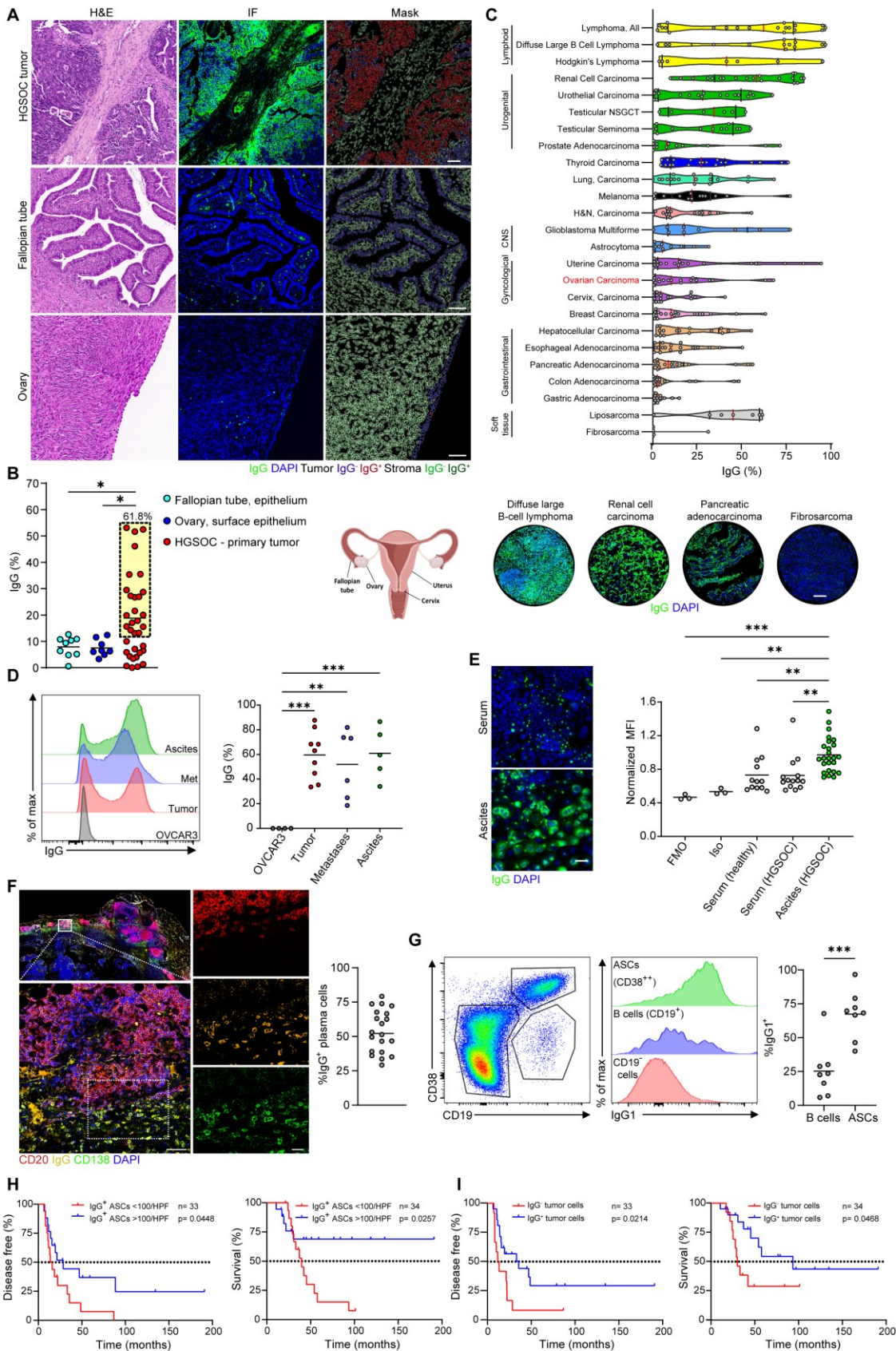
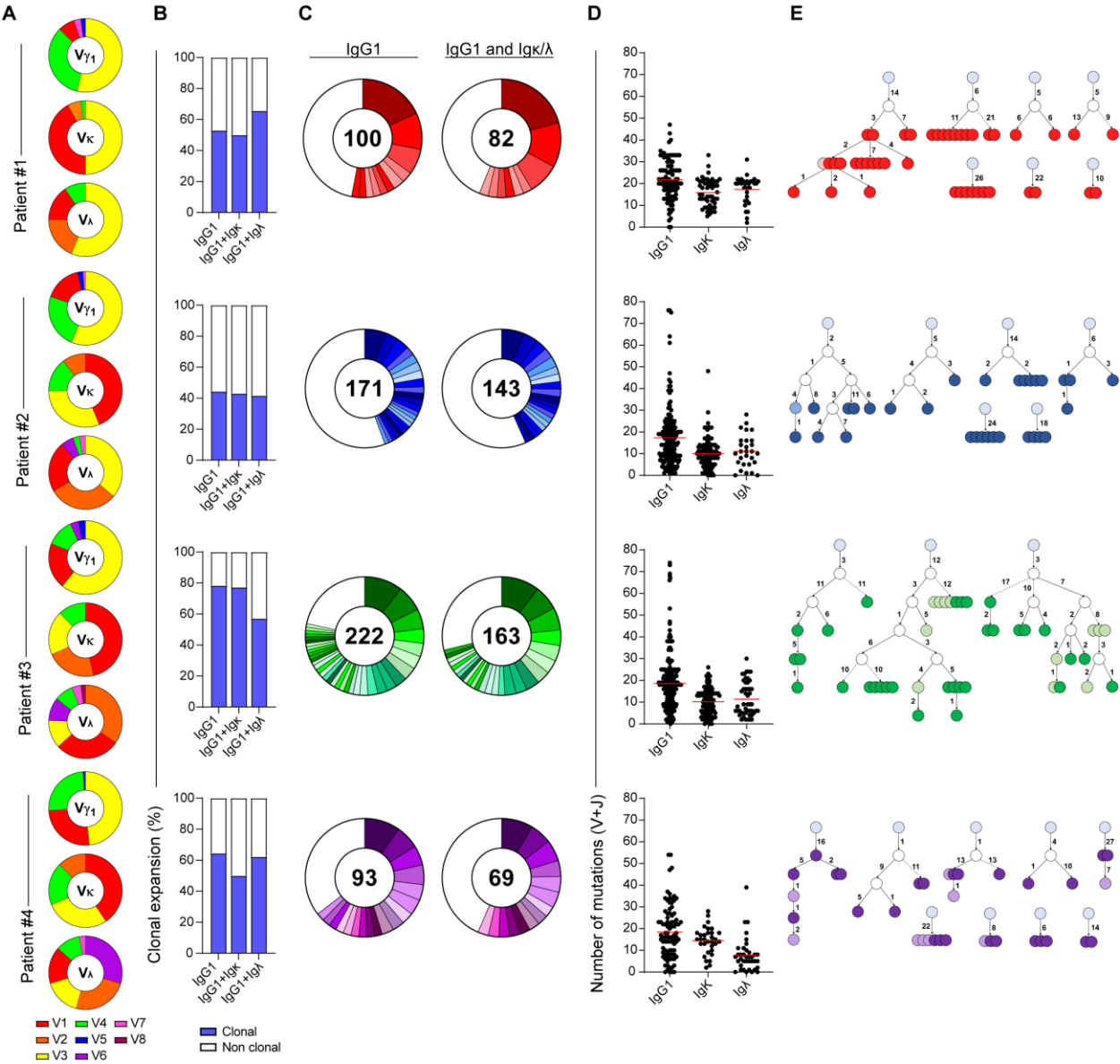


Fig 2



A Isotype control T29 T12 T2

Omental metastasis

OVCA3

Primary tumor

Ascites

Normalized MFI

— Patient #1 — Patient #2 — Patient #3 — Patient #4

B Isotype control T15 T13 T7 T11 T8

OVCA3

IgG DAPI

C Ascites derived polyclonal IgGs

Patients # 1 2 3 4 5 6 7 8 9 10 11 12 13 14 15 16 17 18 19 20 21 22 23 24 25

MMPs

Others

Control

BSA

D Monoclonal IgGs

Patients #1 Patient #2 Patient #3 Patient #4 Control

mAb #

BSA

E mAb T30 mAb T11 mAb T27 mAb T13 mAb T3

mAb T10 mAb T17 mAb T12 mAb T8

OD630

mAb concentration (nM)

— MMP14 — BSA

F Insulin LPS dsDNA HEp-2

ED38 (Positive Control)

Test antibodies

GD01 (Isotype Control)

OD630

mAb concentration (nM)

Fig 4

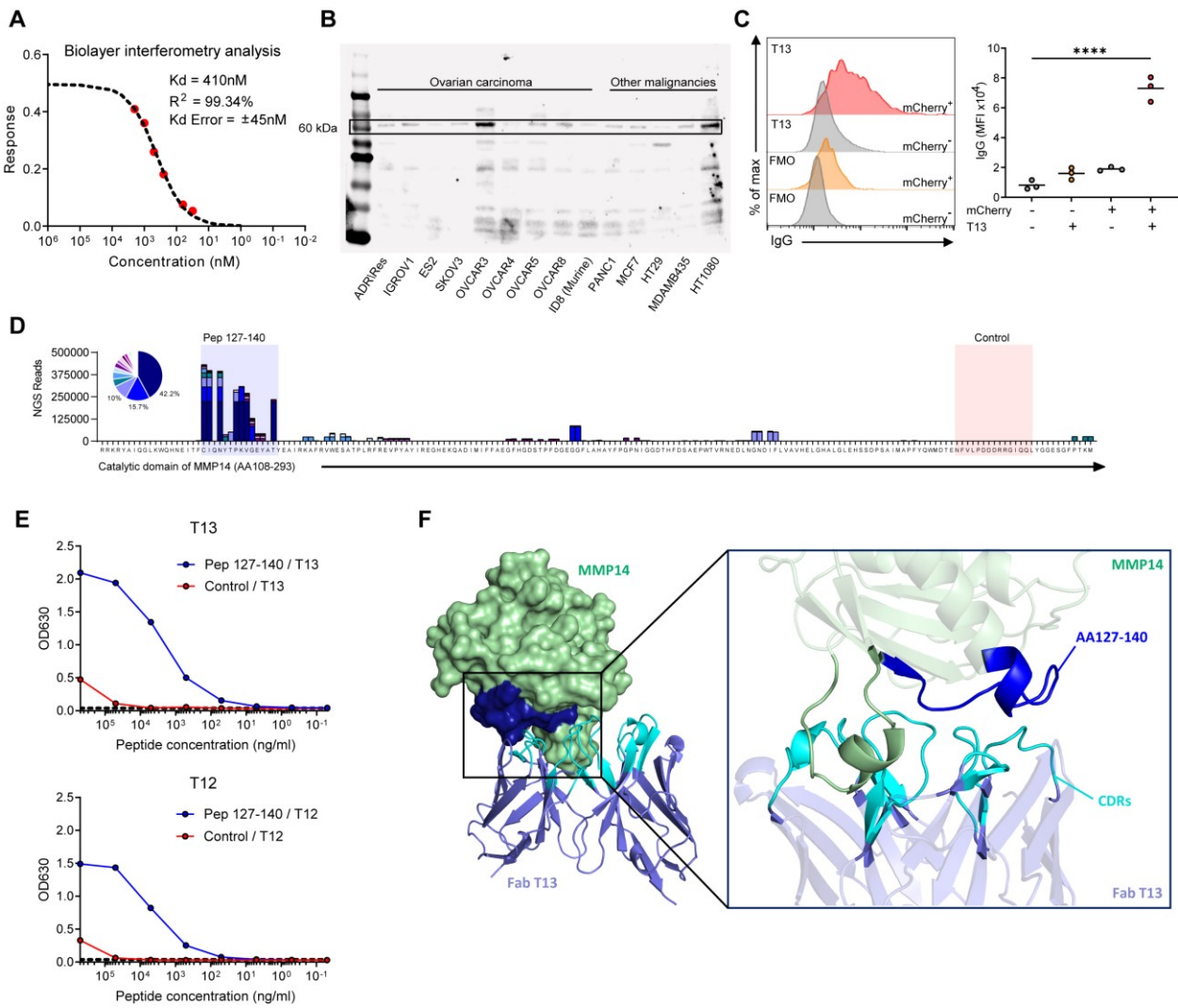


Fig 5

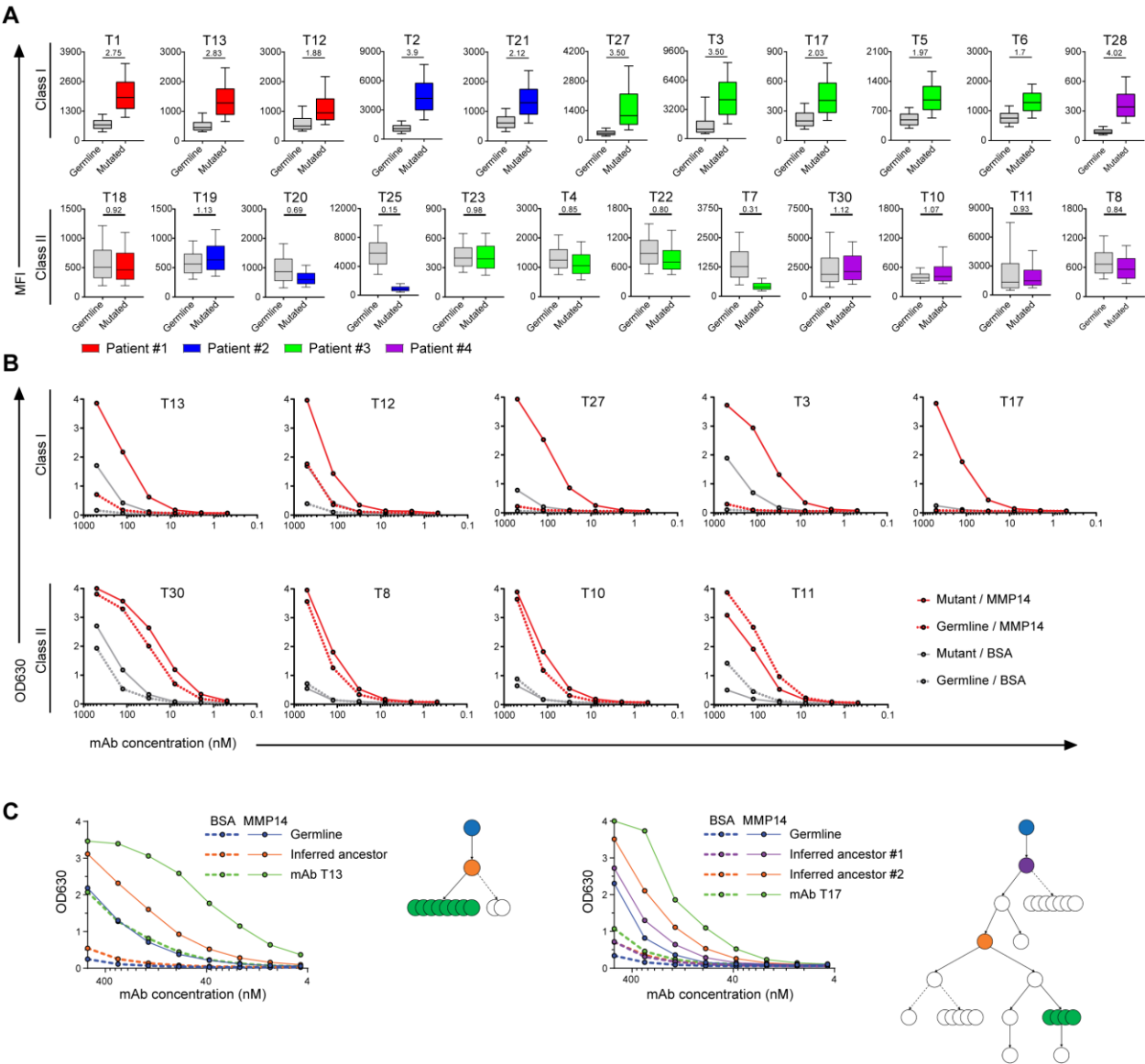


Fig 6

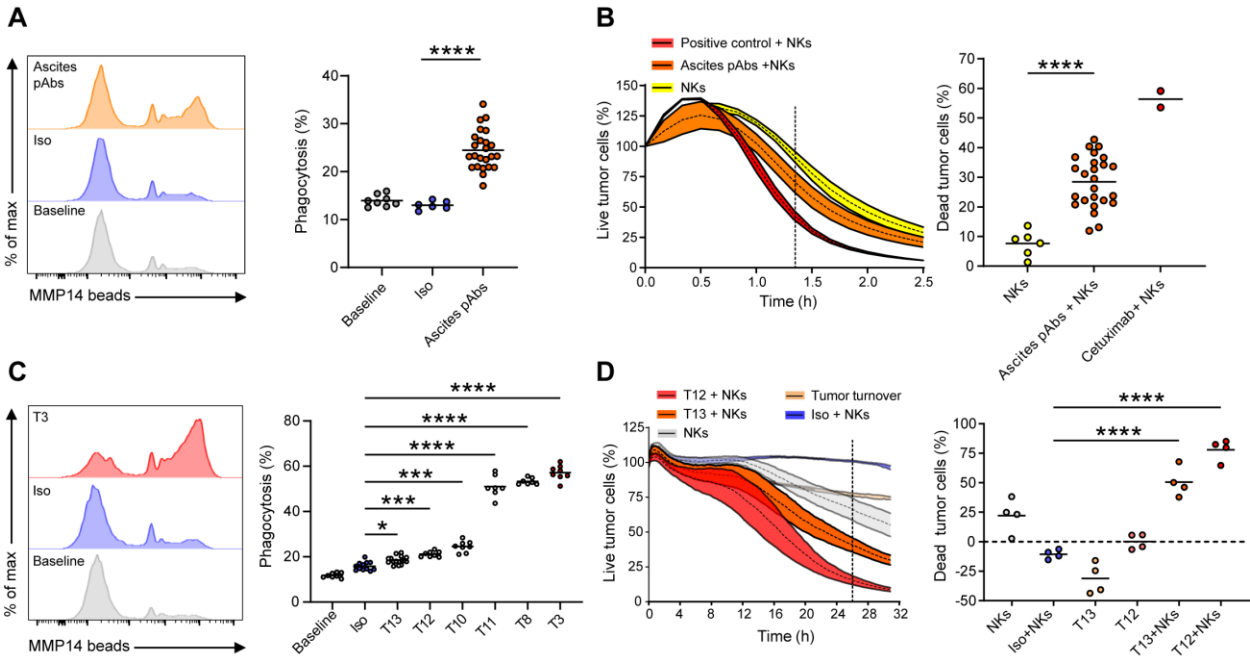


Fig S1

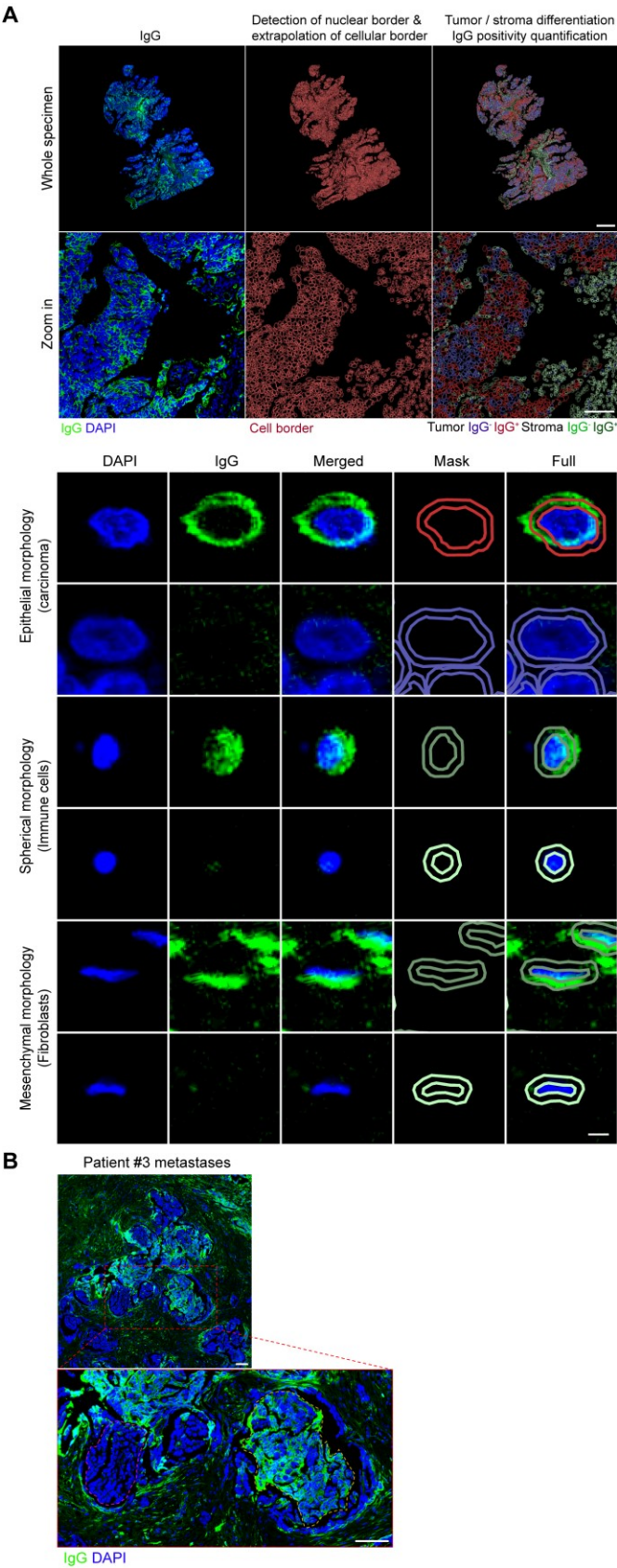


Fig S2

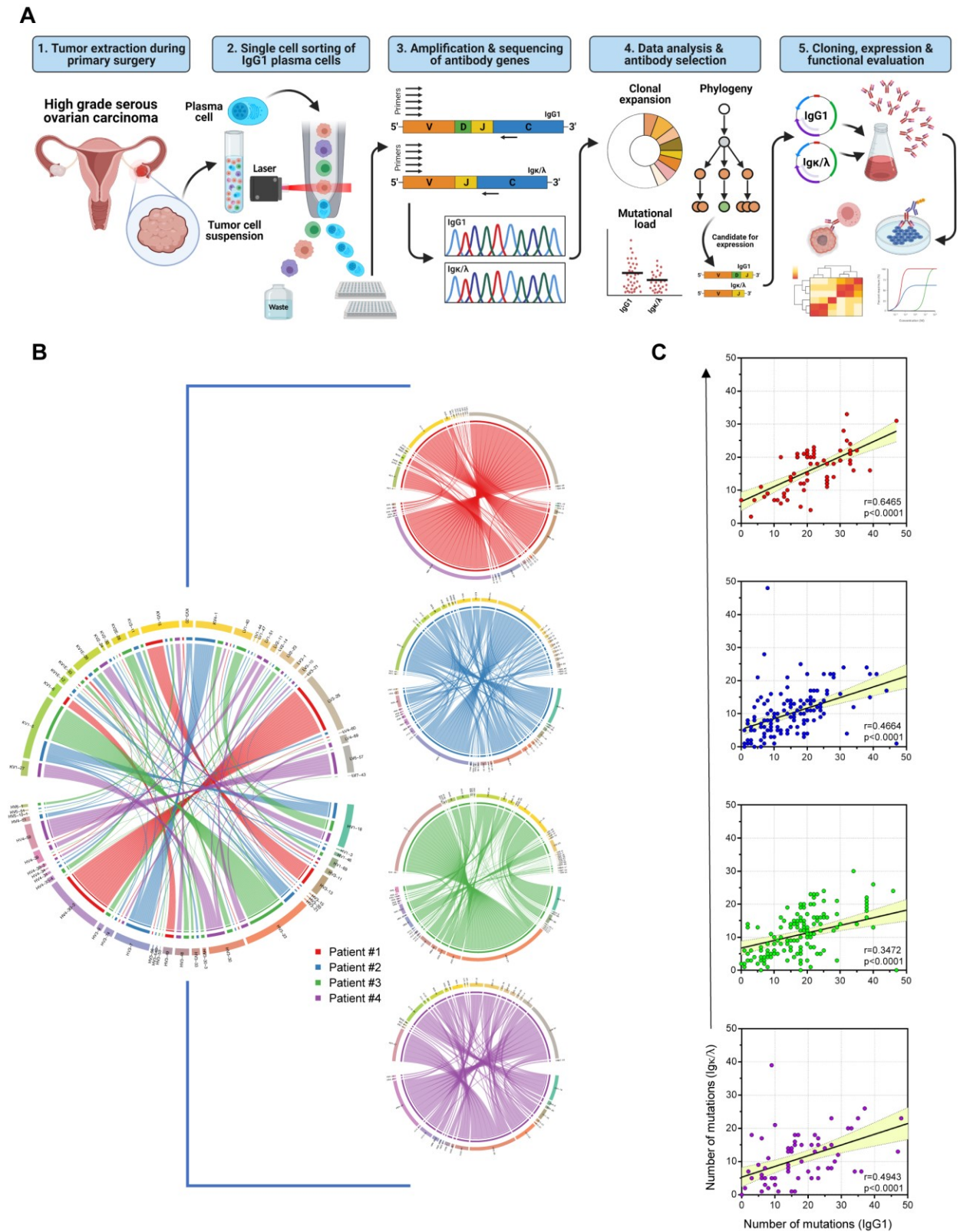


Fig S3

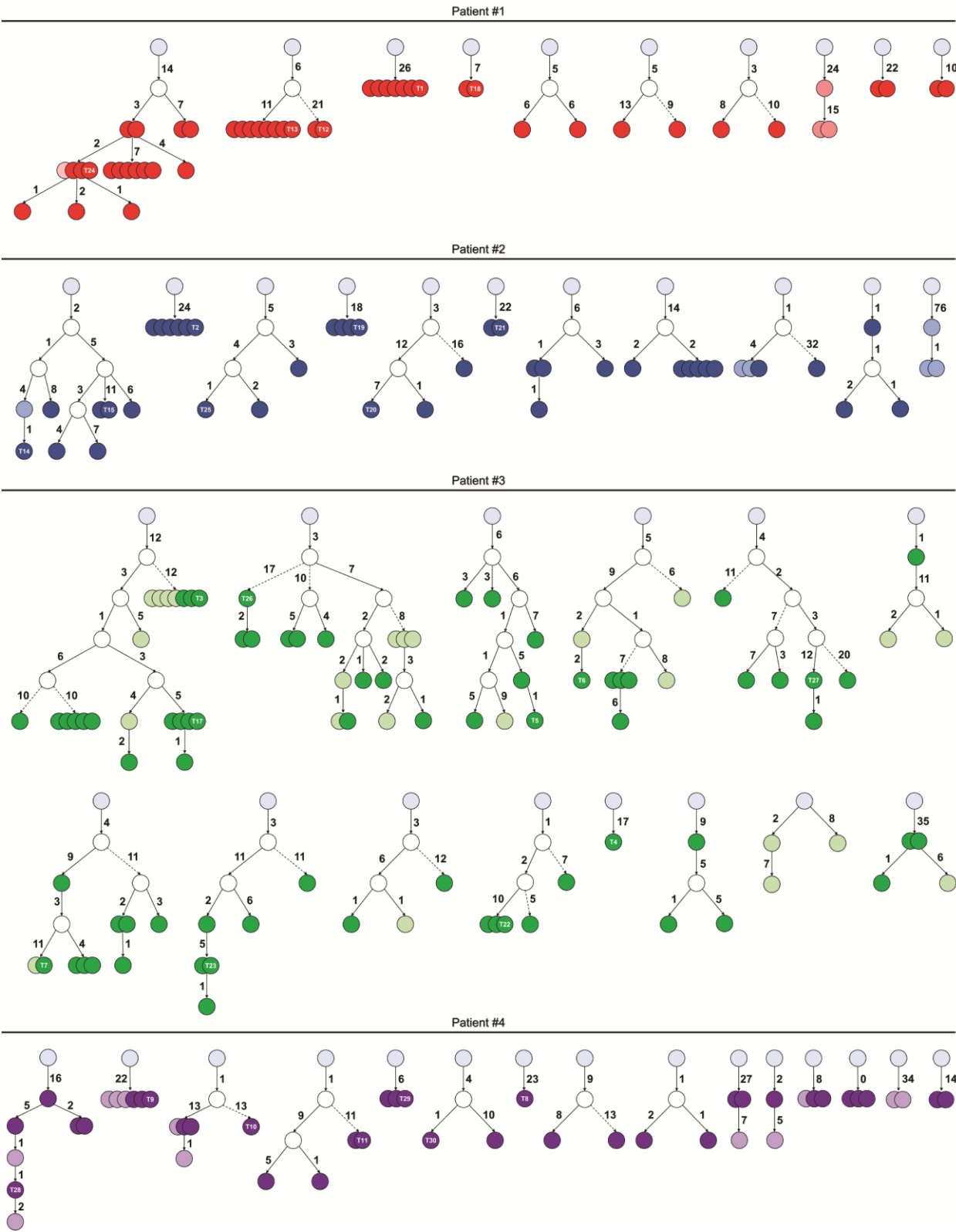


Fig S4

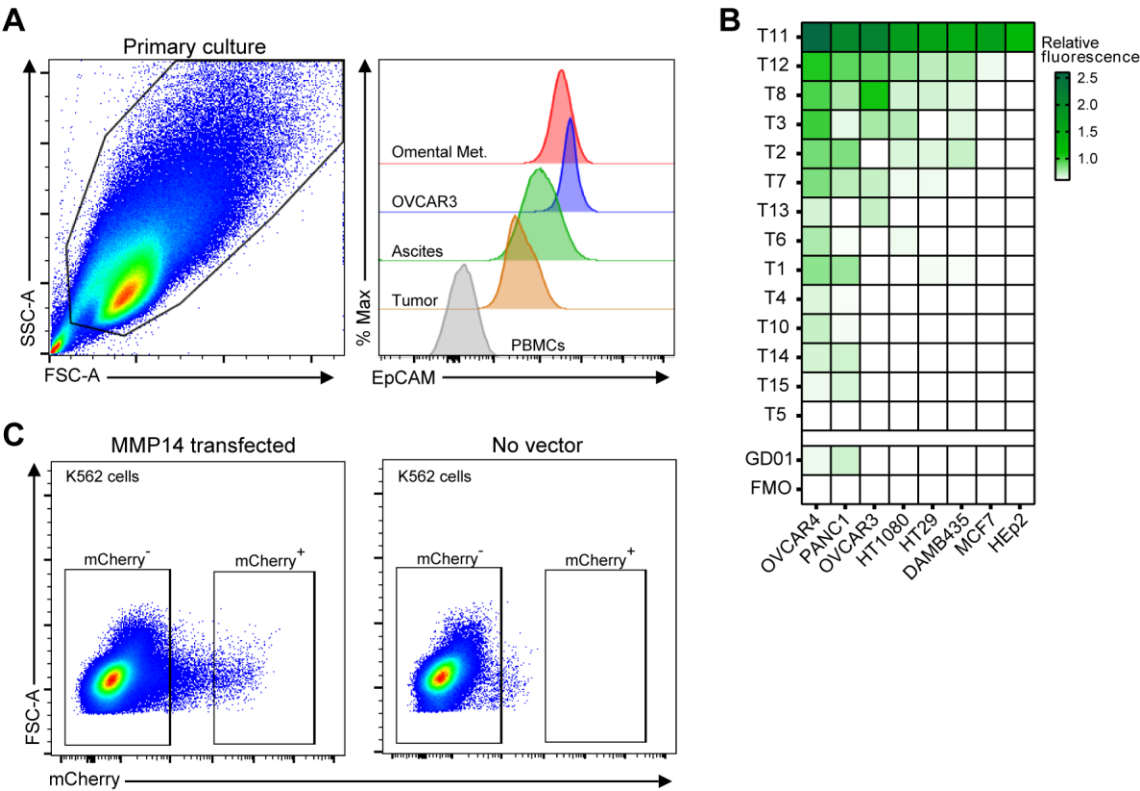


Fig S5

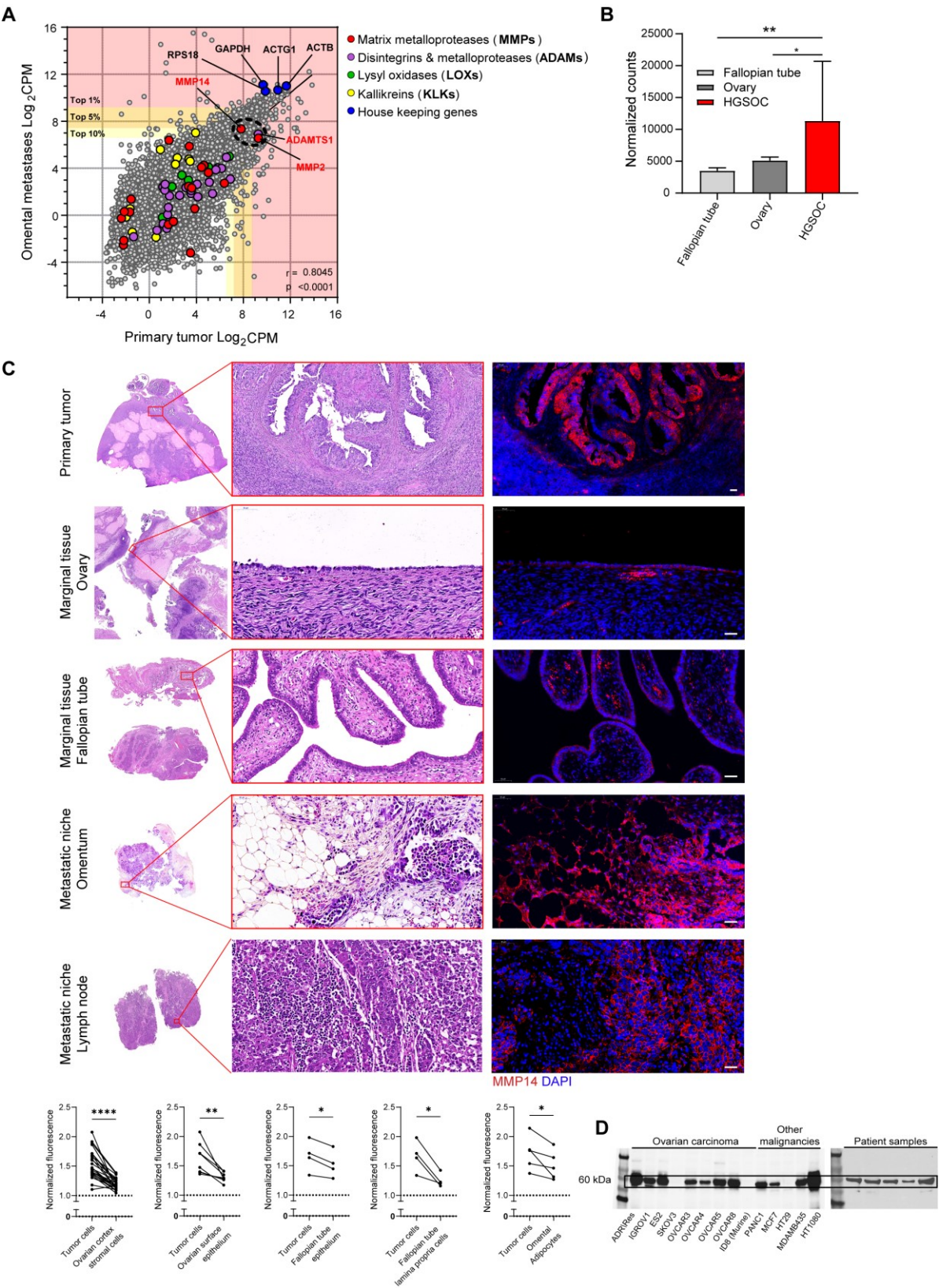


Fig S6

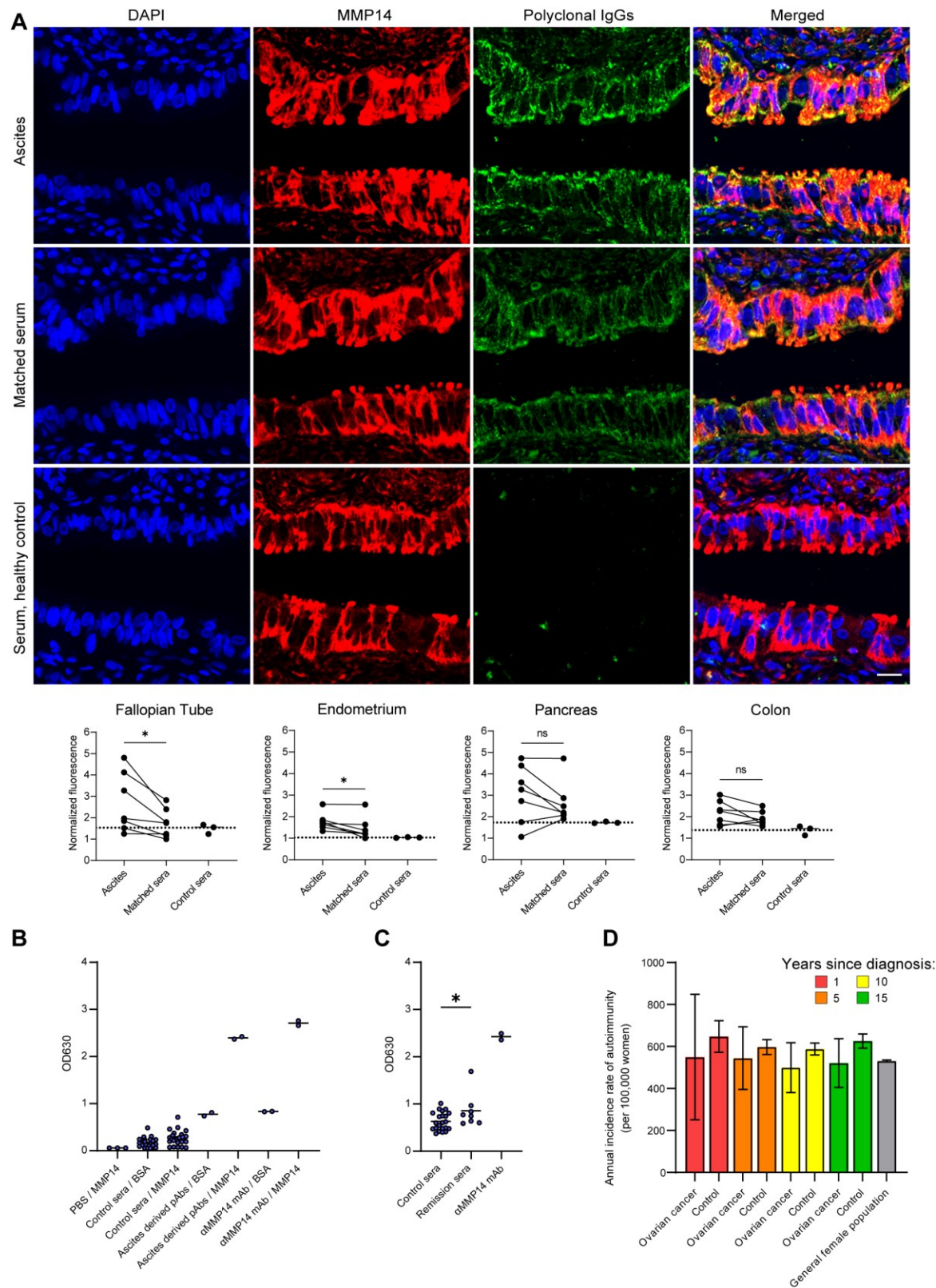


Fig S7

